



Calculation of energy deposition in the pore water of the cements



Silvio Faranda

Advisor: Prof. S. Dulla

Co-advisor: Dott. A. Bonin, (CEA Saclay)

Dipartimento ENERGIA
Politecnico di Torino

MASTER THESIS
Energy and Nuclear Engineering

Academic Year 2020/2021

Table of contents

List of figures.....	ii
List of tables.....	iii
Introduction	1
1 Nuclear waste and pore water in cements	2
1.1 Cemented waste, in metal drums	2
1.2 Pores in cement based materials.....	3
1.2.1 Models for porous cement based materials	4
1.2.2 Pore parameters characteristics	5
1.2.3 Methods to characterize pore structure: LTC, MIP, SEM	6
1.2.3.1 Low temperature calorimetry method (LTC)	6
1.2.3.2 Mercury intrusion porosimetry (MIP).....	6
1.2.3.3 Scanning electron microscopy (SEM).....	7
2 Transport equation	9
2.1 Mean free path	11
2.2 Monte Carlo method.....	12
2.2.1 Scattering model	12
2.2.2 Generation of random path	13
3 Simulation with the PENELOPE code	14
3.1 Total Stopping Power, CSDA, Mean free path: Si and H ₂ O.....	15
3.1.1 Total Stopping Power in Si and H ₂ O	15
3.1.2 Continuous slowing down approximation CSDA range in Si and H ₂ O	17
3.1.3 Mean free path in Si and H ₂ O.....	19
3.2 Simulation 1: Homogeneous, Hybrid, Heterogeneous model	21
3.3 Simulation 2.....	25
3.4 Simulation 3: “Big Layers”	33
4 Simulations with TRIPOLI-4® Transport code	35
4.1 Simulation 1: Layers 0.005 [cm].....	35
4.2 Simulation 2: MACROPORES Layers 0.05 [cm].....	38
5 Spherical Inclusions	41
5.1 TRIPOLI-4®: Spherical Inclusions Simulation.....	42
5.1.1 MODEL A	43
5.1.2 MODEL B	44
5.1.3 MODEL C	45
5.1.4 MODEL D.....	46
5.2 Comparison TRIPOLI-4® with Spherical Inclusions and PENELOPE	48
Conclusions	49

List of figures

Figure 1 Cemented package model [2] 2

Figure 2 Radionuclide decay [20]14

Figure 3 ESTAR Total stopping powers. Linear scale.....15

Figure 4 ESTAR Total stopping powers. Logarithmic scale.....16

Figure 5 PENELOPE CODE Radiative, collision and total stopping powers for electrons in silicon and water as functions of the kinetic energy (solid and dashed curves, respectively). Dot-dashed lines represent the high-energy approximation.....17

Figure 6 PENELOPE CODE CSDA ranges for electrons and positrons in silicon and water as functions of the kinetic energy of the particle.18

Figure 7 Mean free path of Photon and Electron in Si and H₂O.....20

Figure 8 Mean free path of Photon in Si and H₂O with the same density Hybrid model20

Figure 9 Schematic representation of the system, composed of cylinders of water and silica, irradiated by the ¹³⁷Cs source [17].21

Figure 10 Comparison of deposited energy of photons in the Homogeneous, Hybrid and Heterogeneous Model.....22

Figure 11 Comparison of Total deposited energy in Homogeneous, Hybrid and Heterogeneous model.....22

Figure 12 Sum of energy deposited in each adjacent layers in Homogeneous, Hybrid and Heterogeneous model.....23

Figure 13 Comparison of Total deposited energy in H₂O in the Heterogeneous and Homogeneous model ..23

Figure 14 Energy deposited per unit of length in the material consisting of silicon and water in layers of 10 μm thickness over a total length of 100 μm (Heterogeneous model).....24

Figure 15 Spectrum secondary electron (Heterogeneous model)24

Figure 16 Comparison of deposited energy of electrons in the Heterogeneous Model, of ¹³⁷Cs, ⁹⁰Sr, and ⁹⁰Y25

Figure 17 Distribution of thickness layers of Silicon in MODEL C and D26

Figure 18 Deposited energy Photons MODEL A27

Figure 19 Deposited energy Photons MODEL B27

Figure 20 Deposited energy Photons MODEL C28

Figure 21 Deposited energy Photons MODEL D28

Figure 22 Total deposited energy Photons MODEL A, B, C, D.....29

Figure 23 Comparison of Total deposited energy in the Heterogeneous and Homogeneous model29

Figure 24 Comparison of Total deposited energy in H₂O in the Heterogeneous and Homogeneous model ..30

Figure 25 Deposited energy Electrons MODEL A of ¹³⁷Cs, ⁹⁰Sr, and ⁹⁰Y31

Figure 26 Deposited energy Electrons MODEL B of ¹³⁷Cs, ⁹⁰Sr, and ⁹⁰Y31

Figure 27 Deposited energy Electrons MODEL C of ¹³⁷Cs, ⁹⁰Sr, and ⁹⁰Y32

Figure 28 Deposited energy Electrons MODEL D of ¹³⁷Cs, ⁹⁰Sr, and ⁹⁰Y32

Figure 29 Deposited energy “big layers” MODEL A33

Figure 30 Deposited energy “big layers” MODEL B34

Figure 31 Total deposited energy “big layers”34

Figure 32 Configuration model of TRIPOLI-4® (parallel to x-axis)35

Figure 33 Comparison PENELOPE/ TRIPOLI-4® of deposited energy of Photons 0.005 [cm].....36

Figure 34 Comparison PENELOPE/ TRIPOLI-4® of deposited energy of ¹³⁷Cs 0.005 [cm]36

Figure 35 Comparison PENELOPE/ TRIPOLI-4® of deposited energy of ⁹⁰Sr 0.005 [cm].....37

Figure 36 Comparison PENELOPE/ TRIPOLI-4® of deposited energy of ⁹⁰Y 0.005 [cm]37

Figure 37 Comparison PENELOPE/ TRIPOLI-4® of deposited energy of Photons 0.05 [cm].....38

Figure 38 Comparison PENELOPE/ TRIPOLI-4® of deposited energy of ¹³⁷Cs 0.05 [cm]38

Figure 39 Comparison PENELOPE/ TRIPOLI-4® of deposited energy of ⁹⁰Sr 0.05 [cm].....39

Figure 40 Comparison PENELOPE/ TRIPOLI-4® of deposited energy of ⁹⁰ Y 0.05 [cm]	39
Figure 41 Relative error TRIPOLI-4® respect PENELOPE	40
Figure 42 Paraview spherical inclusions uniformly distributed $r=0.1$ [cm] MODEL A	42
Figure 43 Total deposited energy Spherical Inclusions radius = 0.1 [cm]	43
Figure 44 Total deposited energy Spherical Inclusions radius = 0.25 [cm]	44
Figure 45 Deposited energy in water layers MODEL B	45
Figure 46 Total deposited energy Spherical Inclusions radius = 0.5 [cm]	45
Figure 47 Deposited energy in water layers MODEL C	46
Figure 48 Total deposited energy Spherical Inclusions radius = 1 [cm]	47
Figure 49 Deposited energy in water layers MODEL D	47
Figure 50 comparison of the total energy deposited between TRIPOLI-4® with spherical inclusions and PENELOPE.....	48
Figure 51 Relative error	48

List of tables

Table 1 Pore definition.....	4
Table 2 Range of pores and pore structure parameters measured by varying methods	8
Table 3 Radionuclide decay.....	14
Table 4 Total Stopping power	16
Table 5 CSDA range.....	18
Table 6 Radiation length approximation.....	19
Table 7 Mean free path.....	20
Table 8 Thickness layers MODEL C and D	26
Table 9 Percentage reduction of total deposit energy	30
Table 10 Percentage reduction of total deposit energy in H ₂ O	30
Table 11 Configuration “big layers” MODEL A	33
Table 12 Configuration “big layers” MODEL B	33
Table 13 Examples of spherical inclusions generation	42
Table 14 Comparison Volume and Total Energy deposited in Spherical Inclusions radius = 0.1 [cm] and PENELOPE.....	43
Table 15 Comparison Volume and Total Energy deposited in Spherical Inclusions radius = 0.25 [cm] and PENELOPE.....	44
Table 16 Comparison Volume and Total Energy deposited in Spherical Inclusions radius = 0.5 [cm] and PENELOPE.....	46
Table 17 Comparison Volume and Total Energy deposited in Spherical Inclusions radius = 1 [cm] and PENELOPE.....	47

Introduction

In the civil nuclear industry, long-term storage and deep geological disposal of waste require safety assessments to demonstrate the durability of the materials used. Among these materials, concretes are complex and heterogeneous materials that trap large quantities of free interstitial water.

The irradiation of these materials by the confined radionuclides can lead to the accumulation of oxidizing and explosive molecular species.

The molecular hydrogen generated by the radiolysis of water presents risks if its concentration in the air exceeds 4% by volume. The air exchange must be continuous and sufficient in a waste containment storage, so that the atmosphere does not become explosive.

In the framework of studies of the radiolysis in cement-based waste containers, CP2C (Cellule de Protection et Pôle de compétences en Criticité du CEA) laboratory of CEA Saclay makes calculation of the deposited energy in the water contained in the cement. This deposited energy is then used by chemists from CEA to calculate a chemical simulation code the quantity of hydrogen released.

Furthermore, in a sealed vessel, the continuous production of hydrogen will result in an increase in the internal pressure of the cement pores. If the mechanical strength limit is exceeded, an instantaneous failure of the vessel is possible.

Concrete is a composite material consisting of a granular skeleton covered with a cement paste (mixture of water and mineral binder). Cements belong to a category of hydraulic binders composed of calcium silicates and aluminates, called CSH (silica and calcium hydrates). Since water is introduced in excess to facilitate the processing of the material, the cement matrix contains residual alkaline water with a pH between 12 and 14. The most common cement is Portland cement with pore sizes ranging from a few tens of micrometers to a few hundred of micrometers.

In the CP2C laboratory, the radiation shielding unit at the CEA Safety Critical Competence Pole, I studied the deposited energy in the water pores of cement. The calculation of the deposited energy in the water contained in cement is usually performed by homogeneising the cement with the water. The aim of this work is to compare the classical homogeneous model to heterogeneous models of water in cement and to compare results obtained with TRIPOLI-4[®] and with PENELOPE. This led us to use two computer codes of the Monte Carlo type (called PENELOPE and TRIPOLI-4[®]) which deals with the transport of particles (neutrons, photons, electrons and positrons) in matter.

First the calculations are carried out by homogeneising the materials, without taking into account the difference of density. We then studied different configurations taking into account the heterogeneous model. Lastly it was interesting to study the effects of energy depositions in 1D and compare it to a more detailed calculation that takes into account the shape and the position of the pores (stochastic geometry).

From the reasoning developed and the simulations, we will give some ideas for reflection on the energy deposited in the water and therefore which kind of configurations are better to be used.

1 Nuclear waste and pore water in cements

Radioactive waste is generated by the operation and maintenance of nuclear power plants, nuclear fuel cycle plants, research laboratories. This waste must be treated and conditioned in order to have safe disposal. Many countries use cementitious materials (concrete, mortar, etc.) as a containment matrix for storage. The advantage of cementitious materials is greater stability and mechanical support during the storage and disposal of waste. Long-term storage is becoming an important issue in countries where low-level waste disposal is difficult.

Cement has many favorable properties, both chemical and physical, which make it a good matrix for encapsulating radioactive and toxic waste. Chemically cement has a high pH (eg its pore water) and forms hydration products. Cement is also an inexpensive and readily available material. Cement also has good strength when irradiated and the ability to act as a radiation shield. Conventional cementitious materials such as Portland cement and Portland composite cements are very used in waste management systems [1]. Waste can also be affected by radiation and radiolysis products, thus affecting the chemical composition of the "water" in the waste. The energy of the deposited radiation is studied here for three important radionuclides in waste containers: ^{137}Cs , ^{90}Sr , ^{90}Y .

1.1 Cemented waste, in metal drums

Let us take into consideration, Orano, French industry, and analyze the disposal of nuclear waste [2] [3]. Following recycling operations, 96% of spent nuclear fuel (95% uranium + 1% plutonium) can be reused to manufacture new fuel, which will then supply more electricity in turn.

High-level radioactive waste (4%) is vitrified, then conditioned in stainless steel canisters and stored at the La Hague site, pending disposal. This conditioning is certified by 10 safety authorities worldwide. It allows high-level waste to be managed in optimum safety conditions over the very long term, during both the storage and future underground disposal periods.

The metal structures from fuel assemblies (long-lived intermediate-level waste) are compacted and conditioned in steel drums. They are also stored pending disposal.

Waste from fuel cycle operations is conditioned using various technologies, mainly homogenous cement encapsulation or encapsulation by injection, placed in metal containers or concrete shells, then stored or sent to existing surface disposal centers. Orano is constantly developing and optimizing its waste conditioning solutions in order to reduce volumes and conditioning inertia.

Before being able to reprocess the spent fuel to extract the recoverable part, it is essential to separate the fuel, the metal structures that surround it. These metal structures then become waste. Between 1990 and 1995, structural waste from light water reactor fuels was placed in stainless steel drums and blocked by a concrete



Figure 1 Cemented package model [2]

matrix. A small fraction of these packages (about 10%) also contain filters loaded with fine particles of zirconium alloy (the material that the fuel structures are made of) or maintenance waste from the fuel reprocessing process [2] [3].

The waste was collected in a stainless steel drum (Fig. 1) which was then filled with a cement filler. The drum equipped with a first lid was then decontaminated before being equipped with a second welded lid (mechanical protection of the package). Both lids were equipped with stainless steel valves to allow the evacuation of the gases produced by radiolysis.

Property of nuclear waste:

Matrix: cementitious material

Industrial volume of the package: $1.5 \text{ [m}^3\text{]}$

Average weight of the finished package: 3.541 [kg]

Average mass of waste per package: 776 [kg]

Radioactivity determination method:

Neutron measurements were performed on each package to determine the masses of uranium and plutonium, as well as total alpha activity. Some fission products were determined by radiochemical analysis of samples. The radiological inventory was completed using a standard spectrum established by the reactor evolution calculations.

The average activity at the production date is approximately $6.4e^7 \left[\frac{\text{Bq}}{\text{g}} \right]$.

The main contributing radionuclides are:

- α : No predominant radionuclides α ;
- β : ^{55}Fe , ^{60}Co , ^{137}Cs , ^{90}Sr , ^{90}Y , $^{137\text{m}}\text{Ba}$;
- γ : ^{55}Fe , ^{60}Co , ^{137}Cs .

Average heat output: $16 \left[\frac{\text{W}}{\text{pack.}} \right]$ at the production date ($3 \left[\frac{\text{W}}{\text{pack.}} \right]$ after 25 [yers]).

Potentially toxic chemical elements:

- Uranium: $1.2 \left[\frac{\text{kg}}{\text{pack.}} \right]$;
- Lead: $120 \left[\frac{\text{g}}{\text{pack.}} \right]$.
- Other: Included in metal waste, chromium ($86 \left[\frac{\text{kg}}{\text{pack.}} \right]$ coming mainly from stainless steel of cylinder heads), nickel ($56 \left[\frac{\text{kg}}{\text{pack.}} \right]$ coming mainly from nickel alloy structural elements and stainless steel of cylinder heads).

1.2 Pores in cement based materials

The reaction of the cement with water leads to the formation of a porous cement. Different types of pores have been found in hydrated cementitious materials [4]:

- Gel pores ;
- interlayer space of C-S-H (calcium silicate hydrate);
- nanopores;
- micropores;

- intra C-S-H gel;
- inter C-S-H gel;
- capillary pores;
- capillary cavity;
- mesopores.

Pores are the spaces, empty or filled by pore solution, in the hydrated cementitious materials. Various types of pores may be observed in a porous solid (Tab.1).

Table 1 Pore definition

Pore definition	Characteristics
Open pore	Communicates with the surface
Ink-bottle pores	Entry smaller than the actual pore size
Closed pores	No communication with the surface
Open-ended pore	Voids or space between particles

The classification of the pores is a challenge due to the complex and interconnected nature of the pores network in cement pastes. A typical pore size distribution for hydrated cement is about some cm to as small as nm in diameter.

- **Micropores:**
Gel pores: 0.0001 [μm] to 0.001 [μm];
Interlayer pores: 0.001 [μm] to 0.004 [μm];
Capillary pores: 0.001 [μm] to 1 [μm];
- **Macropores:**
Large capillaries: 0.08 [μm] to 10 [μm];
Macropores: 0.2 [μm] to 10000 [μm];

1.2.1 Models for porous cement based materials

We can use the microstructure models in order to describe the complex structure of pores in the hydrated materials. We have different kind of model, for instance, [5] [6] [7].

They have used a granular model for C-S-H, they used two material with different porosity and density [7] [5]. Have been suggested a global structure where them, the two materials were compress together in order to form two kinds of C-S-H gel: high density ($1670 \frac{\text{kg}}{\text{m}^3}$) and low density ($1400 \frac{\text{kg}}{\text{m}^3}$) [5]. According to [6] the water is presented in the C-S-H structure both, intra C-S-H sheets and inter C-S-H particles.

In other cases, it is always considered that the internal and external products could have different porosities, while the hydration products are considered to tend towards a uniform porosity [7]. It should be stressed that the borderline between water sheets of C-S-H and chemically bound water is not clear, as a consequence it is difficult to distinguish between bound and free water in cement based material.

There are not information still about microstructure and accurate measurements to correlate microstructure and pore size. There were been progress regard pore structure by electron microscopy and other methods along with mathematical modelling of microstructure.

Pore structure formation in hydrated cementitious materials is not fully understood. Pore structure is very complex and changes according to the physics and chemical properties of the cement replacement and curing conditions, which makes it difficult to model and describe it in details. The porosity measurements will allow a better understanding of the complex structure of pores.

1.2.2 Pore parameters characteristics

Threshold pore

Threshold pore is related to pore connectivity. It is defined as the minimum diameter of channels that are essentially continuous through the sample [4].

Pore size

The pore size may be defined as the size of the empty or spaces filled with water of hydrated cementitious materials. The radius of a pore is often measured by direct (SEM) or indirect methods.

One way to estimate the average size of a pore radius is through the stereological theory, for hydraulic pores r_h :

$$r_h = \frac{2A_p}{P_p} \quad (1)$$

where:

r_h is the hydraulic radius, [m];

A_p is the cross-section area of pore, [m²];

P_p is the perimeter of pore, [m].

For indirect methods assumptions and theoretical equations are used to determine the size of the pore radius.

Pore volume

Pore volume is the total fraction of spaces: empties and/or filled by the pore solution. The pore volume may be given as the total pore volume, the effective pore volume and the filled pore volume. To calculate pore volume, the density is used. For instance, if we considered the water:

$$V_p = \frac{m_{H_2O}}{\rho_{H_2O}} \quad (2)$$

where:

V_p is the volume of pores, [cm³];

m_{H_2O} is the mass of filled water, [g];

ρ_{H_2O} is the density of water, [$\frac{g}{cm^3}$].

We can have different kind of materials density:

- True density (ρ_{true}): density of the material excluding all pores and voids. It is related to the total volume of pores.
- Apparent density (ρ_{ap}): density of the material including some portion of pores and voids.
- Bulk density (ρ_{bulk}): density of the material including all pores and voids.

1.2.3 Methods to characterize pore structure: LTC, MIP, SEM

The main methods to characterize pore structure of cement pastes are [4]:

- I. Low temperature calorimetry (LTC);
- II. Mercury intrusion porosimetry (MIP);
- III. Scanning electron microscopy (SEM);

1.2.3.1 Low temperature calorimetry method (LTC)

The test estimate important pore structure parameters, e.g. pore thresholds (connectivity), the pore size distribution and the total volume of pores.

The range of detectable pores sizes is from about 0.004 [μm] to 0.080 [μm] in diameter based on [8], 0.004 [μm] to 0.1 [μm] according to [9] and up to 0.400 [μm] from [10].

1.2.3.2 Mercury intrusion porosimetry (MIP)

Mercury intrusion porosimetry (MIP) can be used to evaluate the porosity in cement-based materials. This method consist to forced non-wetting mercury into the porous material at incremental pressures. When a non-wetting liquid is in contact with a solid, the liquid surface develops a characteristic contact angle ($\vartheta > 90^\circ$). The range of pore diameters measured by MIP is from 0.003 [μm] up to 1000 [μm]. The method provides information on the volume of accessible pores and the threshold pore size, i.e. the size of pores providing connectivity. MIP provides information on a large range of pores (from gel to capillary), but capillary condensation methods not [4].

Calculation of pore characteristics

The pressure (p_w) required to force a non-wetting fluid into a circular cross-section capillary of radius r_w is given by the Washburn equation (Washburn equation assumes cylindrical pores):

$$r_w = \frac{-2\gamma \cos \vartheta}{p_w} \quad (3)$$

where:

r_w is the pore radius, [m];

γ is the surface tension solid-liquid, [$\frac{N}{m}$];

ϑ is the contact angle between the liquid and the pore wall, [$degrees$];

p_w pressure applied on mercury to intrude the pore, [$\frac{N}{m^2}$].

The bulk density is determined assuming that no intrusion of mercury into the sample occurs at 0.033 [MPa].

$$\frac{w_{pt}}{\rho_{Hg}} = \frac{w_{ps} - w_s}{\rho_{Hg}} + \frac{w_s}{\rho_{bulk}} \quad (4)$$

Where:

w_{pt} is the weight of penetrometer (sample cell) filled with mercury, [g];

w_s is the weight of dry sample, [g];

w_{ps} is the weight of penetrometer with the sample and mercury (until 0.033 [MPa] the volume), [g];

ρ_{Hg} is the density of mercury, 13.5 [$\frac{g}{cm^3}$];

ρ_{bulk} is the bulk density of sample, [$\frac{g}{cm^3}$].

The volume of pores was calculated using this Equation:

$$V_p = V_{Hg} \frac{\rho_{bulk}}{w_s} \quad (5)$$

where:

V_p is the volume fraction of the pores, [cm^3];

V_{Hg} is the volume of mercury intruded, [cm^3].

Two important pore structure parameters are, the threshold pore size and the total pore volume. The threshold pore size is the size of pores providing entry to the pore network, i.e. connectivity, and it is one of the parameters controlling transport properties of the paste. The total pore volume compares to a broad range of pores and may be related to the mechanical properties of the paste.

MIP does not measure the real pore size distribution, but that of pore-entry sizes. If large pores can be entered only through small pores, they will be registered as small pores.

Also closed pores are not revealed in mercury intrusion curve because they do not have direct contact with the external surface. Lower values for pore size is found when the angle of 117° is used in the Washburn Equation. Studies pointed out, difficulties in the measurements of the surface tension liquid-solid and it also should be stress that it may vary with temperature. In the case of mercury, the literature reports variances from $484.2e^{-7}$ [MPa] at 25 [$^\circ C$] to $472.2e^{-7}$ [MPa] at 50 [$^\circ C$].

1.2.3.3 Scanning electron microscopy (SEM)

Scanning Electron Microscopy (SEM) is widely used to characterize materials. Images obtained by SEM using backscattered electron reproduce a difference in the brightness and contrast which may reflect in the different phases and the pores of hydrated cementitious material. For a plain cement paste sample the darkest parts (black) are the pores, the middle part of the gray scale represents the hydrated phase and the lightest gray levels are dehydrated cement grains. When used for porosity characterization, SEM has advantages over other methods, as they can provide a direct "view" with a high local resolution of the studied material. Other methods (e.g. MIP and LTC) for the porosity assessment are based on theoretical equations and assumptions.

Electron interaction with atom of the sample

For a better understanding of the SEM, it is important to know the nature of the possible interactions between the primary electron (PE) beam and the atom. PE are charged particles and so they interact strongly with the electrically charged particles of the atoms in the sample [11] [12].

When this electron beam reaches the sample, the electrons are scattered many times (multiple scattering) before they are deflected into different ways. The interaction between the electron and the sample's atoms may be inelastic, elastic or electromagnetic radiation. Inelastic (some of energy of primary electron is lost during the interaction) and elastic (no energy is lost during the interaction) interactions are commonly used for the characterization of cement-based materials. The area where the elastic or inelastic interaction takes

place is called the "interaction volume". The size of the interaction volume depends on the energy of electron and the atomic number of the sample. For an element with lighter atomic number, the penetration depth of the primary electrons is higher than that observed for a heavier atomic number. Monte Carlo methods are normally used for simulation in order to obtain a statistical picture of the movement of the electrons in the interaction volume. Emitted lower-energy electrons resulting from inelastic scattering are the secondary electrons (SE). Secondary electrons can be formed by inelastic collisions which results in the emission of low-energy electrons from near the sample's surface. SE is abundant and they are used to give topological and morphological information of the sample. High-energy electrons resulted from an elastic collision of an incident electron, typically with a sample atom's nucleus, are referred to as backscattered electrons (BSE). The energy of BSE will be comparable to that of the incident electrons. These high-energy electrons can escape from areas deeper than secondary electron, so surface topography is not as accurately resolved as for secondary electron imaging. BSE are highly influenced by atomic number of the sample, which is responsible for the phase contrast of the image [13]. For that reason, BSE have been used in the past years to characterize porosity on the cement based materials.

Characterization of porosity by backscattered electrons image and plane of 3D structure

Backscattering electron image has been successfully used in the characterization of the pore structure of cementitious materials [14] [15]. The reproduced contrast and brightness of the backscattered images enable them to have different colors representing different substance in the material. For the quantification of the area of pores is necessary to know the magnification of the image, from that it is possible to calculate the size of each pixel. Once the porosity is isolated, the total area of pores can be calculated:

$$A_{tp} = \frac{A_b}{A_t} \quad (6)$$

where:

A_{tp} is the total area of pores;

A_b is the area of black pixels, [μm^2];

A_t is the total area of grey scale histogram, [μm^2].

There are been listed some important limitations of measurement by SEM [15]. There are been pointed out the influence of the plane of two-dimensional (2D) section of a three-dimensional structure:

- I. Sections through cement grains and aggregates will not generate a real image so the thickness of features will be overestimated;
- II. Connectivity of a 3D structure cannot be deduced from 2D sections.

Table 2 Range of pores and pore structure parameters measured by varying methods

Method	Measured pores	Total size of pore	Pore structure parameters
LTC	0.001 (at $-55\text{ }^{\circ}\text{C}$) to 1.30 (at $-0.05\text{ }^{\circ}\text{C}$) [μm^2];	0.003 to 1 [μm^2]	Threshold pore size, total pore volume and distribution pore size
MIP	0.003 to 1000 [μm^2]	0.003 to 1000 [μm^2]	Threshold pore size and total pore volume
SEM	0.003 to 40 [μm^2] (magnification of 1000)	0.009 to 40 [μm^2] (magnification of 1000)	Total pore volume

2 Transport equation

The transport of radiations (photons, electrons and positrons) within matter is still of great interest. Consequently, interacting with matter, the radiations have different interactions, due to which they begin to lose energy. During these internal interactions in the material, an individual particle creates a new particles, gradually losing energy. This continuous production of particles, due to these internal interactions, is commonly referred to as a shower. Therefore, the production of the shower is nothing more than the representation of the loss of energy by the particle. What we observe in conclusion is a temporal decrease of the energy, initially possessed by the particle interacting with the material, which is deposited gradually in the material.

In order to solve the problems of radiation transport, the integro-differential equation of transport, Boltzmann's linear transport equation is used (eq. 7).

$$\begin{aligned} \frac{1}{v} \frac{\partial \phi(\vec{r}, E, \vec{\Omega}, t)}{\partial t} + \Omega \cdot \nabla \phi(\vec{r}, E, \vec{\Omega}, t) + \Sigma_t(\vec{r}, E) \phi(\vec{r}, E, \vec{\Omega}, t) \\ = \oint d\vec{\Omega}' \int dE' \Sigma_s(\vec{r}, E') \phi(\vec{r}, E', \vec{\Omega}', t) f_s(\vec{r}, E' \rightarrow E, \vec{\Omega}' \cdot \vec{\Omega}) \\ + \oint d\vec{\Omega}' \int dE' \nu \Sigma_f(\vec{r}, E') \phi(\vec{r}, E', \vec{\Omega}', t) \frac{1}{4\pi} \chi(\vec{r}, E) \\ + Q(\vec{r}, E, \vec{\Omega}, t) \end{aligned} \quad (7)$$

In steady-state condition, it becomes:

$$\begin{aligned} \Omega \cdot \nabla \phi(\vec{r}, E, \vec{\Omega}) + \Sigma_t(\vec{r}, E) \phi(\vec{r}, E, \vec{\Omega}) \\ = \oint d\vec{\Omega}' \int dE' \Sigma_s(\vec{r}, E') \phi(\vec{r}, E', \vec{\Omega}') f_s(\vec{r}, E' \rightarrow E, \vec{\Omega}' \cdot \vec{\Omega}) \\ + \oint d\vec{\Omega}' \int dE' \nu \Sigma_f(\vec{r}, E') \phi(\vec{r}, E', \vec{\Omega}') \frac{1}{4\pi} \chi(\vec{r}, E) + Q(\vec{r}, E, \vec{\Omega}) \end{aligned} \quad (8)$$

where:

\vec{r} is the spatial position vector;

E it is the particle energy;

$\vec{\Omega}$ it is the solid angle vector;

t it is the time;

$\phi(\vec{r}, E, \vec{\Omega}, t)$ is the neutron flux, it is the product of v the particles speed $[\frac{cm}{s}]$ and the particles density N $[\frac{neutrons}{cm^3}]$, $[\frac{neutrons}{cm^2s}]$;

Σ_t is the macroscopic total cross section, it is the sum of Σ_s (scattering cross section) and Σ_a (absorption cross section), it is the probability per unit path length to interact in \vec{r} with energy E , $[\frac{1}{cm}]$;

Σ_f is the macroscopic fission cross section, it is the probability per unit path length to do a fission in \vec{r} with energy E , $[\frac{1}{cm}]$;

ν it is the average number of particles emitted by fission reaction;

$\Omega \cdot \nabla \phi(\vec{r}, E, \vec{\Omega})$ it is the streaming term, it is the difference between the particles leaving \vec{r} and the incoming ones for direction $\vec{\Omega}$;

$\Sigma_t(\vec{r}, E)\phi(\vec{r}, E, \vec{\Omega})$ are the particles lost due to scattering and absorption;

$f_s(\vec{r}, E' \rightarrow E, \vec{\Omega}' \cdot \vec{\Omega})$ it is the scattering probability density function;

$\oint d\vec{\Omega}' \int dE' \Sigma_s(\vec{r}, E')\phi(\vec{r}, E', \vec{\Omega}')f_s(\vec{r}, E' \rightarrow E, \vec{\Omega}' \cdot \vec{\Omega})$ represents the particles after scattering with angle $\vec{\Omega}$ and energy E ;

$\chi(\vec{r}, E) dE$ it is the fission emission spectra;

$\oint d\vec{\Omega}' \int dE' \nu \Sigma_f(\vec{r}, E')\phi(\vec{r}, E', \vec{\Omega}') \frac{1}{4\pi} \chi(\vec{r}, E)$ are all neutrons produced by fission reactions in \vec{r} with energy E and in direction $\vec{\Omega}$, it is always zero (our case) except in fissile material;

$Q(\vec{r}, E, \vec{\Omega})$ the particles generated by source.

The integro-differential equation of transport, without fission is:

$$\begin{aligned} \Omega \cdot \nabla \phi(\vec{r}, E, \vec{\Omega}) + \Sigma_t(\vec{r}, E)\phi(\vec{r}, E, \vec{\Omega}) \\ = \oint d\vec{\Omega}' \int dE' \Sigma_s(\vec{r}, E')\phi(\vec{r}, E', \vec{\Omega}')f_s(\vec{r}, E' \rightarrow E, \vec{\Omega}' \cdot \vec{\Omega}) \\ + Q(\vec{r}, E, \vec{\Omega}) \end{aligned} \quad (9)$$

We can write this equation more easily as:

$$\hat{L}\phi = S \quad (10)$$

where

\hat{L} is the losses operator;

S is the source.

Since the transport equation is a linear first order partial differential integral equation, it can be converted into an integral equation by a standard procedure known as the *Method of Characteristics*.

This integral formulation can be useful to understand better the Monte Carlo approach.

$$\begin{aligned} \phi(\vec{r}, E, \vec{\Omega}) = \phi(\vec{r} - s\vec{\Omega}, E, \vec{\Omega}) \exp \left[- \int_0^s ds' \Sigma(\vec{r} - s'\vec{\Omega}, E, \vec{\Omega}) \right] \\ + \int_0^s ds' Q(\vec{r} - s'\vec{\Omega}, E, \vec{\Omega}) \exp \left[- \int_0^{s'} ds'' \Sigma(\vec{r} - s''\vec{\Omega}, E, \vec{\Omega}) \right] \end{aligned} \quad (11)$$

Where

$\exp \left[- \int_0^s ds' \Sigma(\vec{r} - s'\vec{\Omega}, E, \vec{\Omega}) \right]$ is the probability to survive traveling for a distance s .

The quantity $\int_0^{s''} ds'' \Sigma(\vec{r} - s''\vec{\Omega}, E, \vec{\Omega})$ is called *optical path length*:

$$l_{op} = \left[\int_0^{s'} ds'' \Sigma(\vec{r} - s''\vec{\Omega}, E, \vec{\Omega}) \right] \quad (12)$$

Therefore, in conclusion, the probability of a particle to cross a medium without interactions is:

$$p = \exp(-l_{op}) \quad (13)$$

The probability that the first interaction of an incident photon will occur at a certain point between s and $s + ds$ is:

$$P = 1 - \exp(-l_{op}) \quad (14)$$

2.1 Mean free path

Suppose the particles moving inside a random-scattering medium with N molecules per unit volume. We want find the PDF $p(s)$ of the path length s of a particle.

If particles moving inside an infinite medium, the probability that a particle travels a path length s without interacting is:

$$F(s) = \int_s^{\infty} p(s') ds' \quad (15)$$

The probability $p(s)ds$ that the interaction happens when the path length is in the interval $(s, s + ds)$, is equals the product of $F(s)$ (the probability of a particle to cross a medium until s without interactions) and Σds (the probability that the first interaction will occur at a certain point between s and $s + ds$):

$$p(s) = \Sigma \int_s^{\infty} p(s') ds' \quad (16)$$

The solution is ($p(\infty) = 0$),

$$p(s) = \Sigma \exp(-s\Sigma) \quad (17)$$

The mean free path λ is defined as the average path length between collisions:

$$\lambda = \langle s \rangle = \int_0^{\infty} s p(s) ds = \frac{1}{\Sigma} \quad (18)$$

so,

$$\lambda^{-1} = \Sigma \quad (19)$$

The inverse, is the interaction probability per unit path length.

2.2 Monte Carlo method

The transport of radiation in matter can therefore be treated with the Boltzmann linear transport equation. However, this approach can be quite difficult when applied to complex geometries. Therefore the Monte Carlo approach can be useful, when we want to study the transport of radiation in matter in not very simple geometries.

The simulation, where all the interactions made by a particle are simulated in chronological order, is true, so we will have the same results as the solution of the linear transport equation (obviously considering the statistical uncertainties).

The simulation of photon transport is simple because the average number of events in each story is quite small. In fact, a photon story ends after a single photoelectric or pair-producing interaction or after a few Compton interactions.

On the other hand, the simulation of electron transport is much more difficult than that of photons. The main reason is that the average energy loss of an electron in a single interaction is very small. Consequently, when electrons have very large energy they need a lot of interactions before being absorbed into the medium. So simulating electrons when the average number of collisions per interaction is not too large, that's fine. That is, when the electron sources have low energies (around 100 keV) or fairly simple geometries such as very thin layers. On the other hand, for high energies and / or thick geometries, the average number of electron collisions becomes very high until it is stopped, as a consequence also the computational time becomes very high.

The history (path) of a particle is nothing more than a random sequence of free flights. Flights end with an interaction event. In each event the particle changes its direction of movement and loses energy. In order to simulate the random paths an interaction model is needed, a set of differential cross sections (DCS). DCSs determine the probability distribution functions (PDF) of random variables: free path, type of interaction, energy loss and angular deflection. The main drawback of the Monte Carlo approach is its haphazard nature. Obviously, the results are therefore influenced by statistical uncertainties. This problem can be easily solved by increasing the number of events and using variance reduction techniques.

2.2.1 Scattering model

Considering a particle with energy E travel in a material, in each interaction it can lose energy E' and/or change its direction of movement (by change angular deflection by scattering angle $\vec{\Omega}$ and azimuthal angle ϕ).

Assuming two main interaction mechanisms (elastic and inelastic).

The scattering model is specified by the differential cross sections:

$$\frac{d^2\sigma(E, \vartheta, E')}{d\Omega dE'} \quad (20)$$

where $d\Omega$ is a solid angle element in the direction (ϑ, ϕ) . The total cross sections is:

$$\sigma_T(E) = \int_0^E dE' \int_0^\pi 2\pi \sin \vartheta d\vartheta \frac{d^2\sigma(E, \vartheta, E')}{d\Omega dE'} \quad (21)$$

The PDFs of the polar scattering angle and the energy loss are:

$$p(E, \vartheta, E') = \frac{2\pi \sin \vartheta}{\sigma_T(E)} \frac{d^2\sigma(E, \vartheta, E')}{d\Omega dE'} \quad (22)$$

The azimuthal scattering angle is uniformly distributed in $(0, 2\pi)$, i.e.,

$$p(\phi) = \frac{1}{2\pi} \quad (23)$$

2.2.2 Generation of random path

The particle path has a initial position $r = (x, y, z)$, energy E and direction $\vec{d} = (u, v, w)$.

The next states will be r_n, E_n, \vec{d}_n , where they represent the states at the n-th scattering event (with n=0 at initial state, n=1 to the next state and so on).

The random variables that are sampled from the PDFs are:

- I. the length s of the free path to the next collision;
- II. the scattering mechanism;
- III. the change in direction;
- IV. the energy loss in the collision.

The length of free path, is distributed according to the PDF:

$$p(s) = \lambda_T^{-1} \exp(-s/\lambda_T)$$

Random variable of s are generated by using the sampling formula:

$$s = -\lambda_T \ln \xi \quad (24)$$

ξ is a random number uniformly distributed in the interval $(0, 1)$.

The next interaction happens at the position:

$$r_{n+1} = r_n + s\vec{d}_n \quad (25)$$

The polar scattering angle ϑ and the energy loss E' are sampled from the distribution $p(E, \vartheta, E')$, Eq. 22.

The azimuthal scattering angle is generated, according to the uniform distribution in $(0, 2\pi)$, as $\phi = 2\pi\xi$.

After the interaction, the energy of the particle is lower, $E_{n+1} = E_n - E'$, and the direction of movement after the interaction $\vec{d}_{n+1} = (\dot{u}, \dot{v}, \dot{w})$, is obtained by doing a rotation of $\vec{d}_n = (u, v, w)$.

The simulation of the path is done again by doing these steps. The path is over when the particle comes out of the material or when the energy decreases to an energy E_{abs} , which we consider to be the energy where either the particle stops or is absorbed.

3 Simulation with the PENELOPE code

PENELOPE (PENetration and Energy Loss of Positrons and Electrons) is a Monte Carlo type energy transport simulation code based on the probability of interaction (photoelectric effect, Compton effect, pair production effect) in well-defined geometries.

This code does not know how to deal with incident photons with an energy of less than 1 [keV] and secondary electrons with an energy of less than 100 [eV]. With an energy of 100 [eV], the code considers the particles absorbed in matter. From this code it is possible to calculate the number of electrons per unit area and the absorbed dose as well as representing the distribution of the dose as a function of the distance traveled by the electrons.

Simulation input parameters

The input parameters are as follows:

- the number of trace particles. The larger it is, the more reliable the result, but the longer the simulation time;
- the initial energy of the radiation (photons, electrons or protons) and / or the energy spectrum;
- the dimensions of the source (thickness, internal and external radius, coordinates of the center of the source, direction of the beam, angle of aperture);
- the type of interaction, the number of interaction events (photoelectric effect, Compton effect, torque production, elastic and inelastic collisions, etc.);
- the time of the simulation;
- analysis calculation modules.

In our case, the primary particles are photons and electrons (see fig. 2) and the material is made up of several layers, homogeneous and concentric of a given composition, heterogeneous, and radius of a given thickness. Layers are a way to represent the pores in 1D and walls of our porous systems. Primary particles are emitted from a cylindrical source. The source and structure of the material are symmetrical about a Z axis. The isotopes we use for our simulations are: ¹³⁷Cs, ⁹⁰Sr, ⁹⁰Y. We use ¹³⁷Cs with γ and β decay, ⁹⁰Sr and ⁹⁰Y with β decay (see tab 3).

Table 30.1. Revised November 1993 by E. Browne (LBNL).

Nuclide	Half-life	Type of decay	Particle		Photon	
			Energy (MeV)	Emission prob.	Energy (MeV)	Emission prob.
²² Na	2.603 y	β^+ , EC	0.545	90%	0.511 Annih. 1.275 100%	
⁵⁴ Mn	0.855 y	EC			0.835 100% Cr K x rays 26%	
⁵⁶ Fe	2.73 y	EC			Mn K x rays: 0.00590 24.4% 0.00649 2.86%	
⁵⁷ Co	0.744 y	EC			0.014 9% 0.122 86% 0.136 11% Fe K x rays 58%	
⁶⁰ Co	5.271 y	β^-	0.316	100%	1.173 100% 1.333 100%	
⁶⁵ Ge	0.742 y	EC			Ga K x rays 44%	
\rightarrow ⁶⁸ Ga		β^+ , EC	1.899	90%	0.511 Annih. 1.077 3%	
⁹⁰ Sr	28.5 y	β^-	0.546	100%		
\rightarrow ⁹⁰ Y		β^-	2.283	100%		
¹⁰⁶ Ru	1.020 y	β^-	0.039	100%		
\rightarrow ¹⁰⁶ Rh		β^-	3.541	79%	0.512 21% 0.622 10%	
¹⁰⁹ Cd	1.267 y	EC	0.063 e ⁻ 0.084 e ⁻ 0.087 e ⁻	41% 45% 9%	0.088 3.6% Ag K x rays 100%	
¹¹³ Sn	0.315 y	EC	0.364 e ⁻ 0.388 e ⁻	29% 6%	0.392 65% In K x rays 97%	
¹³⁷ Cs	30.2 y	β^-	0.514 e ⁻ 1.176 e ⁻	94% 6%	0.662 85%	
¹³³ Ba	10.54 y	EC	0.045 e ⁻ 0.075 e ⁻	50% 6%	0.081 34% 0.356 62% Ca K x rays 121%	
²⁰⁷ Pb	31.8 y	EC	0.481 e ⁻ 0.975 e ⁻ 1.047 e ⁻	2% 7% 2%	0.569 98% 1.063 75% 1.770 7% Pb K x rays 78%	
²²⁸ Th	1.912 y	6 α : 3 β^- :	5.341 to 8.785 0.334 to 2.246		0.239 44% 0.583 31% 2.614 36%	
(\rightarrow ²²⁶ Ra \rightarrow ²²⁶ Rn \rightarrow ²¹⁸ Po \rightarrow ²¹⁸ Pb \rightarrow ²¹⁴ Pb \rightarrow ²¹⁴ Po)						
²⁴¹ Am	432.7 y	α	5.443 5.486	13% 85%	0.060 36% Np L x rays 38%	

Figure 2 Radionuclide decay [20]

Table 3 Radionuclide decay

Photon and Electron radiation			
¹³⁷ Cs	¹³⁷ Cs	⁹⁰ Sr	⁹⁰ Y
$\gamma = 0.660$ [MeV]	$\beta = 0.500$ [MeV]	$\beta = 0.546$ [MeV]	$\beta = 2.280$ [MeV]

3.1 Total Stopping Power, CSDA, Mean free path: Si and H₂O

Before proceeding with the simulations, it might be useful to evaluate some important parameters. It would be interesting to calculate the total stopping power, the mean free path and the CSDA range (continuous slowing down approximation), in the following materials: Silicon and Water (materials that we consider in order to build our model of water pores in cement). This will allow us to already do some important considerations on the deposit of energy on the various layers that will make up our model.

3.1.1 Total Stopping Power in Si and H₂O

- **Collision stopping power (Electrons):** average rate of energy loss per unit path length, due to Coulomb collisions that result in the ionization and excitation of atoms;
- **Radiative stopping power:** average rate of energy loss per unit path length due to collisions with atoms and atomic electrons in which bremsstrahlung quanta are emitted. Important only for electrons;
- **Total stopping power:** for electrons, the sum of the collision and radiative stopping powers;

The total stopping power can be determined by the ESTAR program established by the NIST (National Institute of Standards and Technology) for electrons with energy between 10^{-3} [MeV] and 10^3 [MeV] in water and silica (figs 3 and 4) [16].

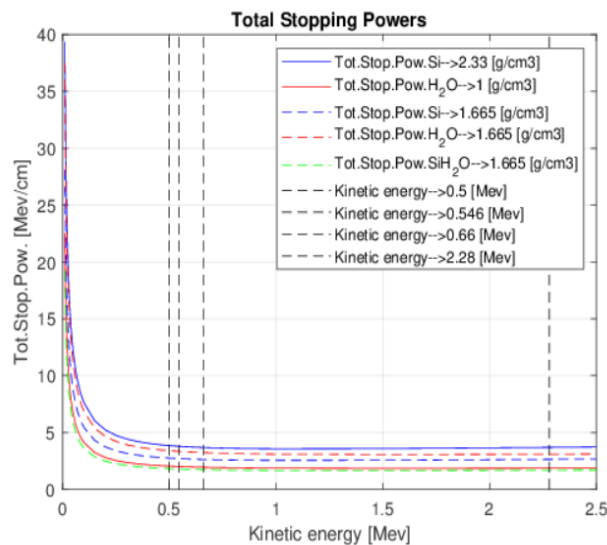


Figure 3 ESTAR Total stopping powers. Linear scale

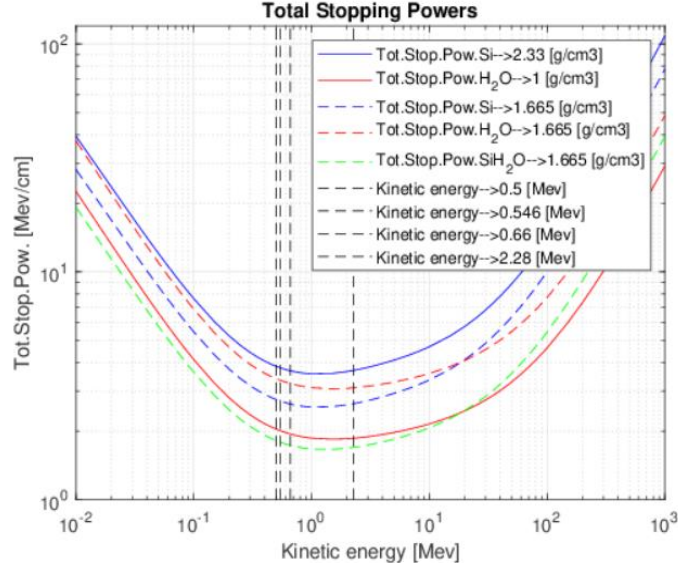


Figure 4 ESTAR Total stopping powers. Logarithmic scale

We have plot the total stopping power for different density, because, we have simulated different models. Homogeneous model in which, we have a unique material with density $1.665 \left[\frac{g}{cm^3} \right]$. Hybrid model in which, we have two material silicon and water with the same density $1.665 \left[\frac{g}{cm^3} \right]$. Heterogeneous model in which, we have two material silicon and water with density $2.330 \left[\frac{g}{cm^3} \right]$ and $1.000 \left[\frac{g}{cm^3} \right]$, respectively.

Table 4 Total Stopping power

MATERIAL	DENSITY [g/cm ³]	TOTAL STOPPING POWER [MeV/cm]			
		$\gamma=0.660$ [MeV]	$\beta=0.500$ [MeV]	$\beta=0.546$ [MeV]	$\beta=2.28$ [MeV]
Si	2.330	3.6791	3.8492	3.7862	3.6930
Si	1.665	2.6290	2.7506	2.7056	2.6390
H ₂ O	1.000	1.9420	2.0410	2.0060	1.8600
H ₂ O	1.665	3.2334	3.3983	3.3400	3.0969
SiH ₂ O	1.665	2.8821	3.0253	2.9737	2.8255

So we can say that the stopping power gives the average energy loss per unit of path length (see table 4). As a consequence, when an electron with energy E crosses a distance ds inside a material, it loses an (average) energy $dE = -S(E)ds$, where:

$$S(E) = S_{in} + S_{br} = -\frac{dE}{ds} \quad (26)$$

is the total (S_{in} =collisional+ S_{br} =radiative) stopping power. Fig. 5 compares the radiative, collision and total stopping powers in silicon and water for electrons. As can be seen from the graph, for high energies, the total stopping power can be approximated to the radiative stopping power. So electrons with very high energies radiate photons with high energies, with a strong reduction in energy in each event. On the other hand as we can see from the graph, the radiative stopping power is proportional to the energy for really high energies.

$$S_{br}(E) \cong \frac{E}{X_0} \quad (27)$$

where the distance X_0 is the *radiation length*.

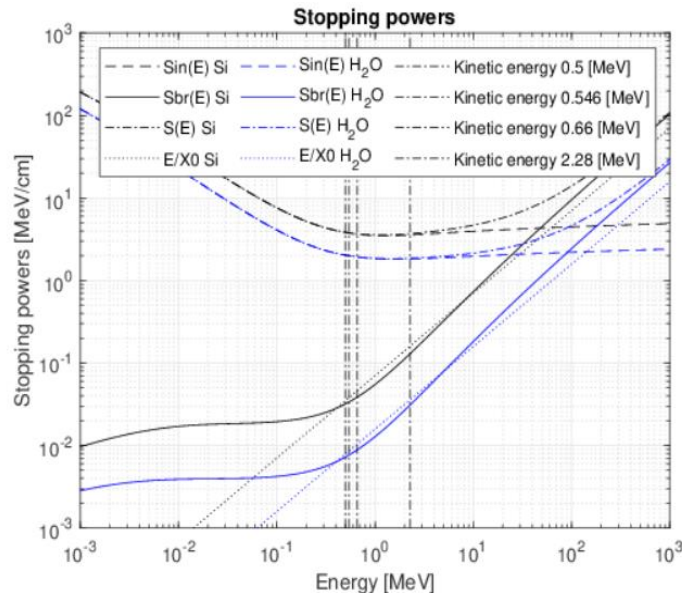


Figure 5 PENELOPE CODE Radiative, collision and total stopping powers for electrons in silicon and water as functions of the kinetic energy (solid and dashed curves, respectively). Dot-dashed lines represent the high-energy approximation.

As we can see from the graphs 3, 4 and 5, the total stopping power of silicon is larger than the total stopping power of water. As a consequence we expect a larger energy deposit in the silicon layers than in the water layers.

While, when we use the hybrid model, that is, when we use the same density of $1.665 \left[\frac{g}{cm^3} \right]$ [17] for both silicon and water, the total stopping power in water becomes greater than the total stopping power in silicon. As a consequence we expect a greater energy deposit in the water layers than in the silicon layers with the hybrid model.

3.1.2 Continuous slowing down approximation CSDA range in Si and H₂O

It is a very close approximation to the average path length travelled by a charged particle as it slows down to rest, calculated in the continuous-slowng-down approximation. In this approximation, the rate of energy loss at every point along the track is assumed to be equal to the total stopping power.

So it assumes that particles lose energy in a continuous way.

Energy-loss fluctuations are neglected. The CSDA range is obtained integrating the inverse of the total stopping power respect to energy.

$$CSDA = \int_{E_{abs}}^E \frac{d(E')}{S(E')} \quad (28)$$

E_{abs} is the energy where the particles are absorbed. It is necessary to remember that the CSDA interval gives the average path length, the true paths lengths oscillate around the average CSDA. Fig. 6 shows the CSDA ranges for electrons in silicon 2.330 $\left[\frac{g}{cm^3}\right]$ and water 1.000 $\left[\frac{g}{cm^3}\right]$, from PENELOPE, this information is useful, for example, to estimate the maximum penetration depth of a bundle (see table 5).

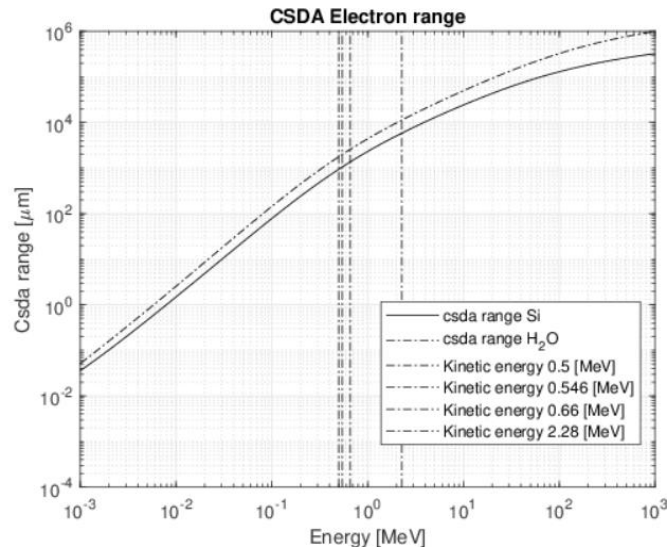


Figure 6 PENELOPE CODE CSDA ranges for electrons and positrons in silicon and water as functions of the kinetic energy of the particle.

Table 5 CSDA range

MATERIAL	DENSITY $[g/cm^3]$	CSDA Electron [cm]		
		$\beta=0.500$ [MeV]	$\beta=0.546$ [MeV]	$\beta=2.28$ [MeV]
Si	2.330	0.0943	0.1063	0.5860
H ₂ O	1.000	0.1777	0.2006	1.1345

The CSDA links the path length s and the average energy E , and takes a simple form when the energy is very high. Under these conditions, the losses of radiative energy are the most important and the approximation (27) can be applied.

$$S(E) \cong S_{br}(E) \cong \frac{E}{X_0} \quad (29)$$

Electrons with initial energy $E(0)$ after travelling a path length s have an average energy $E(s)$.

The CSDA:

$$s = \int_{E(s)}^{E(0)} \frac{d(E')}{S(E')} \cong X_0 \ln \left(\frac{E(0)}{E(s)} \right) \quad (30)$$

So:

$$E(s) = E(0) \exp \left(-\frac{s}{X_0} \right) \quad (31)$$

Hence, when the electron travels a distance X_0 the energy decrease by a factor $e \sim 2.71$.

Table 6 Radiation length approximation

MATERIAL	DENSITY [g/cm ³]	X_0 [cm]		
		$\beta=0.500$ [MeV]	$\beta=0.546$ [MeV]	$\beta=2.28$ [MeV]
Si	2.330	0.1299	0.1442	0.6174
H ₂ O	1.000	0.2450	0.2722	1.2258

As we can see from the tab. 6, the higher is the energy, the closer the approximation of X_0 is to the CSDA.

3.1.3 Mean free path in Si and H₂O

It is the average distance travelled by a moving particle (such as an atom, a molecule, a photon, an electron) between successive impacts (collisions), which modifies its direction or energy or other particle properties. From the PENELOPE code we can compare the mean free path of photons and electrons (figs 7 and 8).

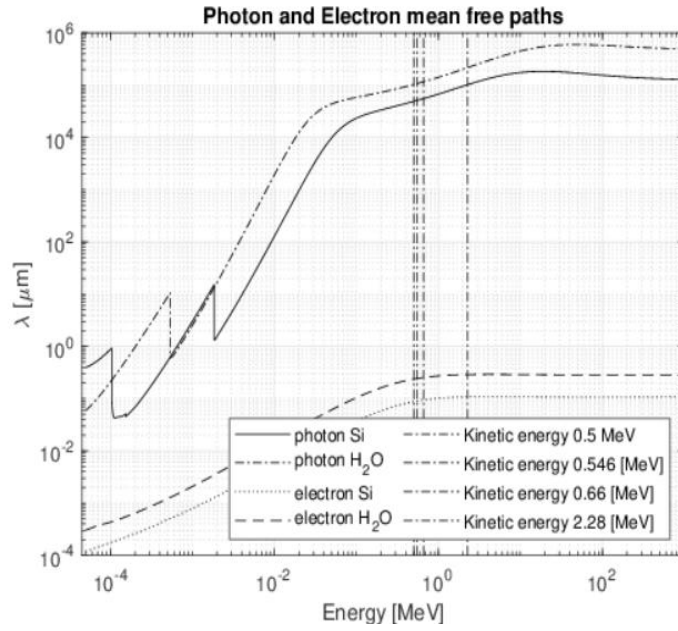


Figure 7 Mean free path of Photon and Electron in Si and H₂O

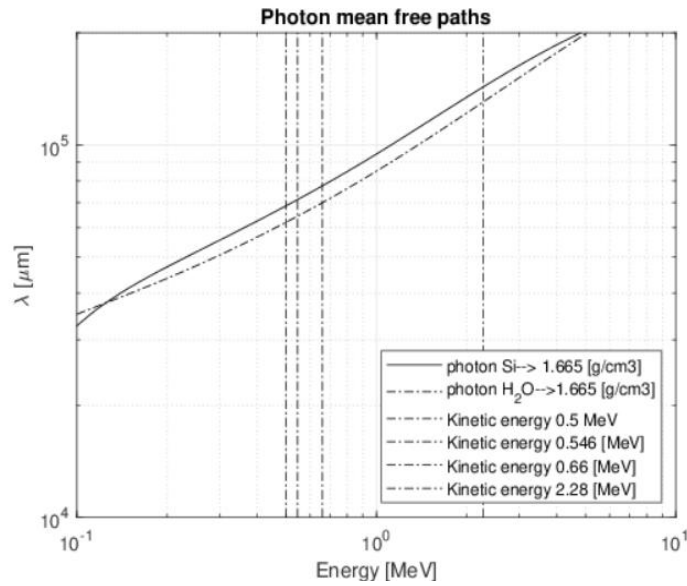


Figure 8 Mean free path of Photon in Si and H₂O with the same density Hybrid model

Table 7 Mean free path

MATERIAL	Photon [cm]		Electron [cm]	
	$\gamma=0.660$ [MeV]	$\beta=0.500$ [MeV]	$\beta=0.546$ [MeV]	$\beta=2.28$ [MeV]
Si $\left(2.330 \left[\frac{\text{g}}{\text{cm}^3}\right]\right)$	5.5019	$8.7489e - 6$	$9.0003e - 6$	$1.0830e - 5$
H ₂ O $\left(1.000 \left[\frac{\text{g}}{\text{cm}^3}\right]\right)$	11.5550	$2.3658e - 5$	$2.4276e - 5$	$2.8910e - 5$

The photon and electron mean free paths (see tab. 7) in silicon is smaller than the photon and electron mean free paths in water. While, when we use the hybrid model, that is, when we use the same density of $1.665 \left[\frac{g}{cm^3} \right]$ for both silicon and water, the photon mean free path in silicon becomes greater than the photon mean free path in water. We will therefore expect a greater penetration of photons than electrons but with a lower energy deposition (par. 3.1.1).

3.2 Simulation 1: Homogeneous, Hybrid, Heterogeneous model

The studied system (fig. 9) is composed of two materials, silicon and water (respectively with density $2.330 \left[\frac{g}{cm^3} \right]$ and $1.000 \left[\frac{g}{cm^3} \right]$) subjected to photon and electron radiation (see tab 3). It was therefore considered a material composed alternatively of 10 cylindrical layers, each of $10 \left[\mu m \right]$. Total thickness of silicon $50 \left[\mu m \right]$ and total thickness of H_2O $50 \left[\mu m \right]$.

The energy deposited on each layer was studied, taking into account different configurations:

- Homogeneous model: 10 alternating cylindrical layers, the first layer is Si, each of $10 \left[\mu m \right]$, homogenized in volume, with an average density of $1.665 \left[\frac{g}{cm^3} \right]$;
- Hybrid model: 10 alternating cylindrical layers, the first layer is Si, each of $10 \left[\mu m \right]$, with an average density of $1.665 \left[\frac{g}{cm^3} \right]$;
- Heterogeneous model: 10 alternating cylindrical layers, the first layer is Si, each of $10 \left[\mu m \right]$, density of silicon $2.330 \left[\frac{g}{cm^3} \right]$ and density of water $1.000 \left[\frac{g}{cm^3} \right]$.

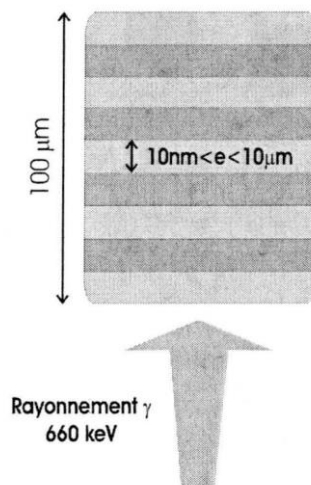


Figure 9 Schematic representation of the system, composed of cylinders of water and silica, irradiated by the ^{137}Cs source [17].

The graph shown in fig. 10 represent the energy deposits of photons in each layer, respectively in the homogeneous, hybrid and heterogeneous model, each point on the x-axis corresponds to the middle of a layer, obtained with PENELOPE.

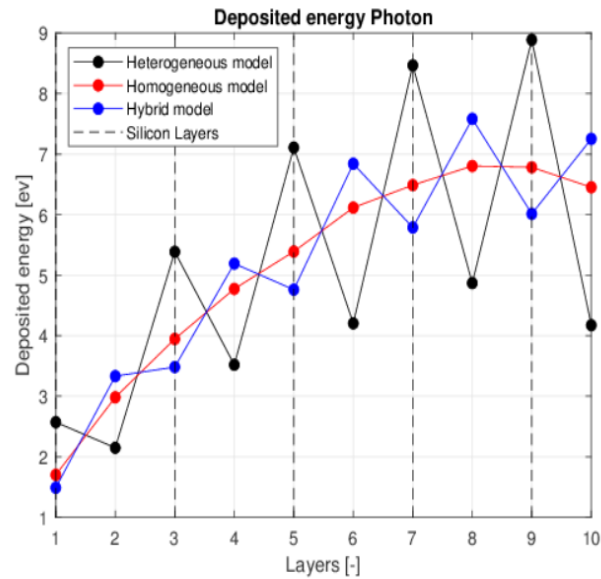


Figure 10 Comparison of deposited energy of photons in the Homogeneous, Hybrid and Heterogeneous Model

In the homogeneous model we have a uniform increase in the deposited energy, and this is what we expect. On the other hand, both in the hybrid and in the heterogeneous model the energy deposit in the silicon and water layers is different. Comparing the hybrid and the heterogeneous model it is interesting to notice that the energy deposit is opposite. In the heterogeneous model the energy deposit in the silicon layers is higher than the energy deposit in the water layers, as we would expect.

The fig. 11, shows the integrated energy deposited over the entire volume.

The fig. 12, compare the sum of the deposited energy in two adjacent layers obtained with the heterogeneous, homogeneous and hybrid model, each point on the x-axis corresponds to the sum of two slices (point 1 sum of one and second layer, point 2 sum of the second and third layer, and so on ..).

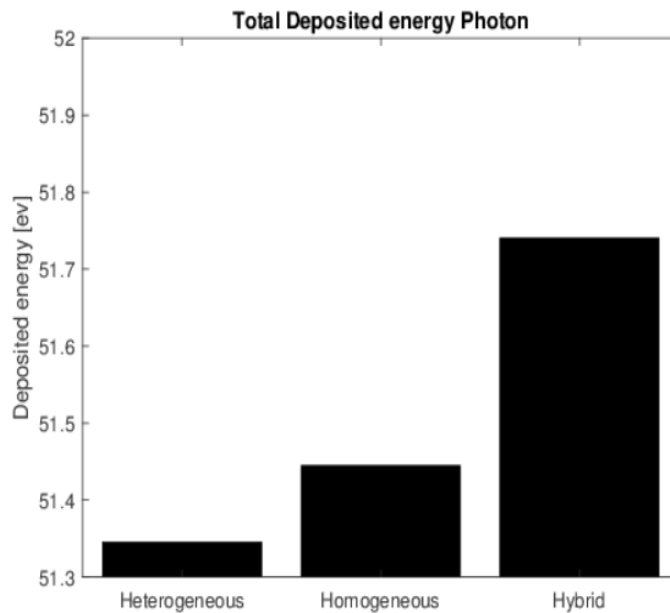


Figure 11 Comparison of Total deposited energy in Homogeneous, Hybrid and Heterogeneous model

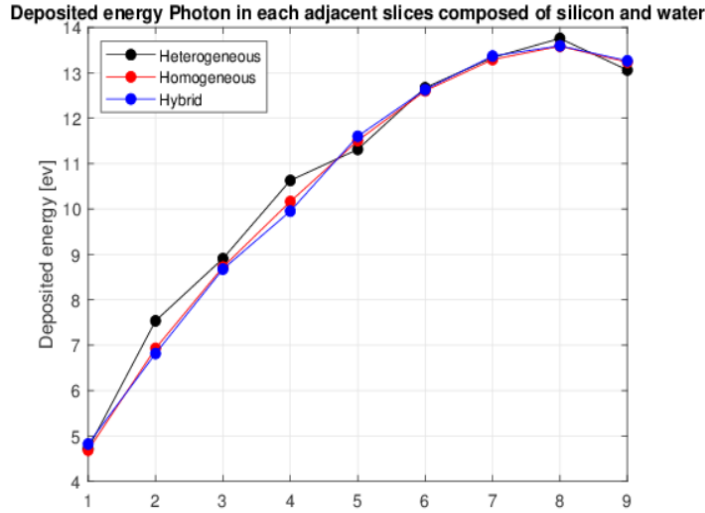


Figure 12 Sum of energy deposited in each adjacent layers in Homogeneous, Hybrid and Heterogeneous model

As we see from figs. 11 and 12, both the total energy deposit over the entire volume and the sum of the energy deposit in the respective adjacent layers, is almost equal in the homogeneous, hybrid and heterogeneous models. What we can say in conclusion is that both the homogeneous and the hybrid model, about our aims, can be defined as "conservative". That is, the energy deposit is higher in these two models.

It is also useful to evaluate the total energy deposit on the water layers, and compare it in the heterogeneous and homogeneous model (see fig. 13).

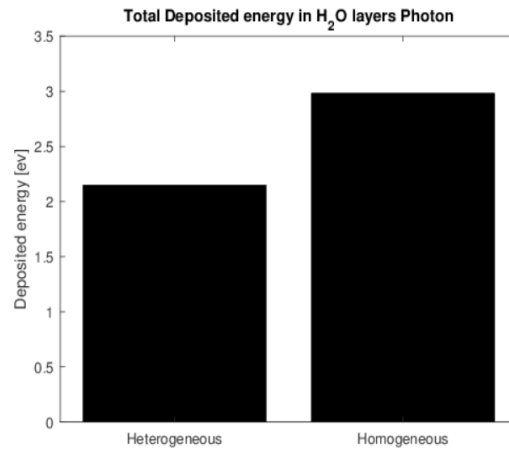


Figure 13 Comparison of Total deposited energy in H₂O in the Heterogeneous and Homogeneous model

As we can see from figure 13, we have an energy deposit in the H₂O layers that is 27.94 % lower than in the homogeneous model.

Figure 14 shows the energy deposited per unit of length and per photon γ expressed in $\left[\frac{keV}{cm}\right]$. This linear energy deposit is readily related to the mass absorption coefficient.

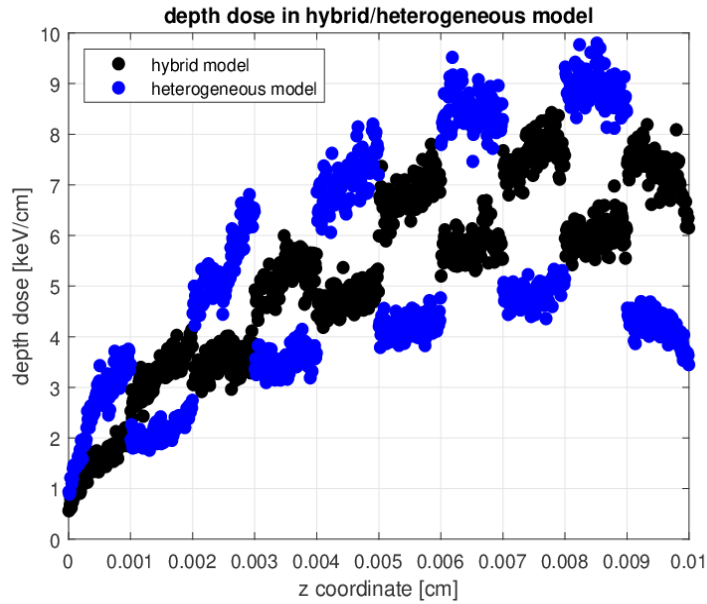


Figure 14 Energy deposited per unit of length in the material consisting of silicon and water in layers of $10\ \mu\text{m}$ thickness over a total length of $100\ \mu\text{m}$ (Heterogeneous model)

We observe that the deposition of the dose is heterogeneous, the amount of energy deposited increases with the distance of penetration, both in silicon and in water. This is due to the fact that the electronic equilibrium is not reached for the whole thickness of the simulated system (the electronic equilibrium calculations require material thickness greater than the mean free path of the secondary electrons). The energy deposited in the silicon is always greater than that deposited in the water, in the heterogeneous model, as verified in the previous calculations.

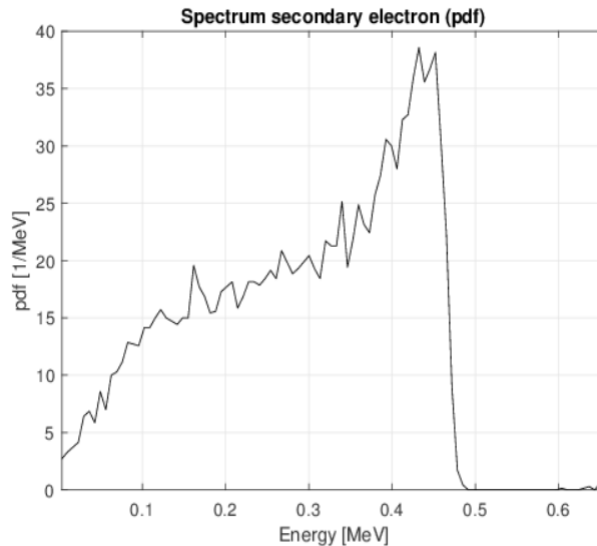


Figure 15 Spectrum secondary electron (Heterogeneous model)

The energy spectrum of secondary electron is shown in figure 15. As we can see, most electrons are emitted with an energy of $0.5\ \text{MeV}$, below the energy of the incident photons $0.66\ \text{MeV}$.

The graph shown in fig. 16 represents the energy deposits of electron in each layer, with the heterogeneous model, respectively of the ^{137}Cs , ^{90}Sr , and ^{90}Y , each point on the x-axis corresponds to the middle of a layer.

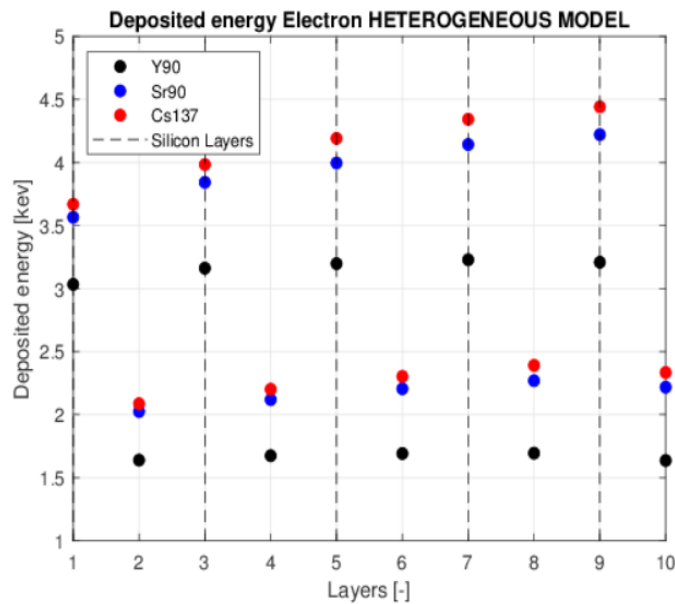


Figure 16 Comparison of deposited energy of electrons in the Heterogeneous Model, of ^{137}Cs , ^{90}Sr , and ^{90}Y

As expected, the energy deposit is much higher, on the order of [keV], compared to the energy deposit due to photonic radiation. The energy store is higher, respectively, in the case of ^{137}Cs , ^{90}Sr , and ^{90}Y .

This too was quite predictable, in fact the total stopping power, initially equal in the three cases (see figs. 3 and 4), as the kinetic energy decreases it increases a lot in the case of the ^{137}Cs , ^{90}Sr , this leads to a greater slowdown and therefore to a greater energy deposit.

The CSDA range of electrons ($0.500 [MeV]$) is of around $900 [\mu m]$ in Si (see tab. 5). That would we observe if the material had 1000 layers instead of 10 (qualitatively) is decrease of the curve towards the end of the CSDA range.

3.3 Simulation 2

The studied system is composed always of two materials, silicon and water (respectively with density $2.330 [\frac{g}{cm^3}]$ and $1.000 [\frac{g}{cm^3}]$) subjected to photonic (^{137}Cs) and electron radiation (^{137}Cs , ^{90}Sr , and ^{90}Y). This time it was considered a material composed alternately of cylindrical layers of different thickness, total thickness $1000 [\mu m]$. The total thickness of silicon is $500 [\mu m]$ and the total thickness of H_2O is $500 [\mu m]$, for all the simulated configurations (MODEL A, MODEL B, MODEL C, MODEL D). The first layer of each model is Si.

The energy deposited on each layer was studied, taking into account different configurations:

- MODEL A: 99 alternating cylindrical layers, each of $10 [\mu m]$;
- MODEL B: 20 alternating cylindrical layers, each of $50 [\mu m]$;
- MODEL C: 22 alternating cylindrical layers (Tab.8);
- MODEL D: 22 alternating cylindrical layers (Tab. 8);

Table 8 Thickness layers MODEL C and D

LAYERS	MATERIAL	MODEL C thickness [μm]	MODEL D thickness [μm]
1	Si	50	20
2	H ₂ O	50	50
3	Si	20	30
4	H ₂ O	50	50
5	Si	30	10
6	Si	10	20
7	H ₂ O	50	50
8	Si	60	20
9	H ₂ O	50	50
10	Si	30	30
11	H ₂ O	50	50
12	Si	50	30
13	H ₂ O	50	50
14	Si	20	20
15	H ₂ O	50	50
16	Si	80	80
17	H ₂ O	50	50
18	Si	10	10
19	H ₂ O	50	50
20	Si	90	100
21	H ₂ O	50	50
22	Si	50	130
TOTAL THICKNESS		1000	1000

The figure 17 shows the thickness distribution of the model C and D.

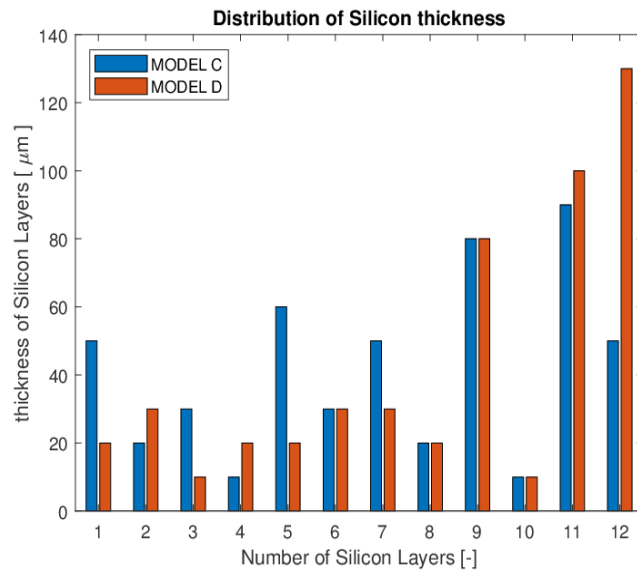


Figure 17 Distribution of thickness layers of Silicon in MODEL C and D

The MODEL D has the end slices of silicon with the greater thickness respect the other models, so we expect that in the MODEL D there will be the bigger deposited energy (fig. 22).

The deposited energy of photons (0.660 [MeV]) of each model are show in figs. 18, 19, 20 and 21.

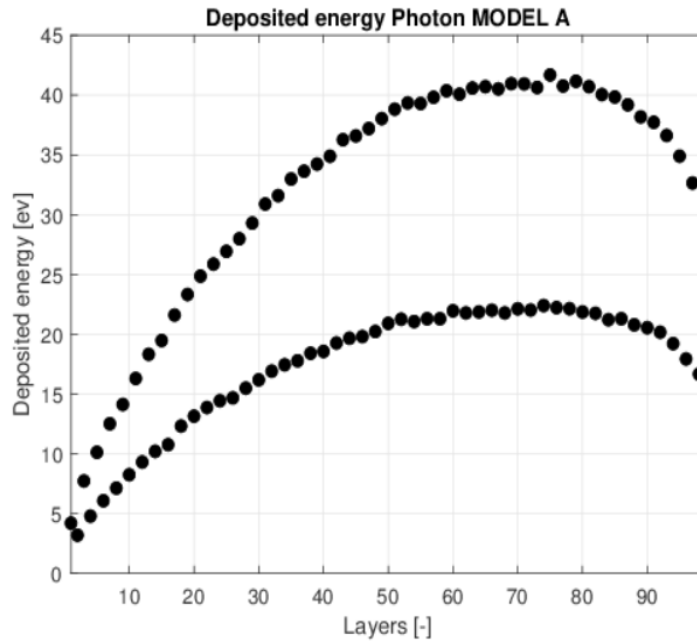


Figure 18 Deposited energy Photons MODEL A

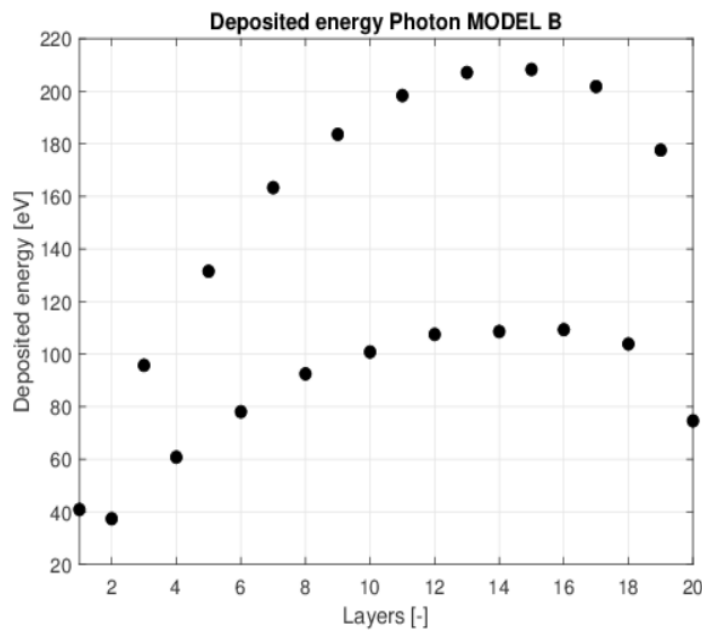


Figure 19 Deposited energy Photons MODEL B

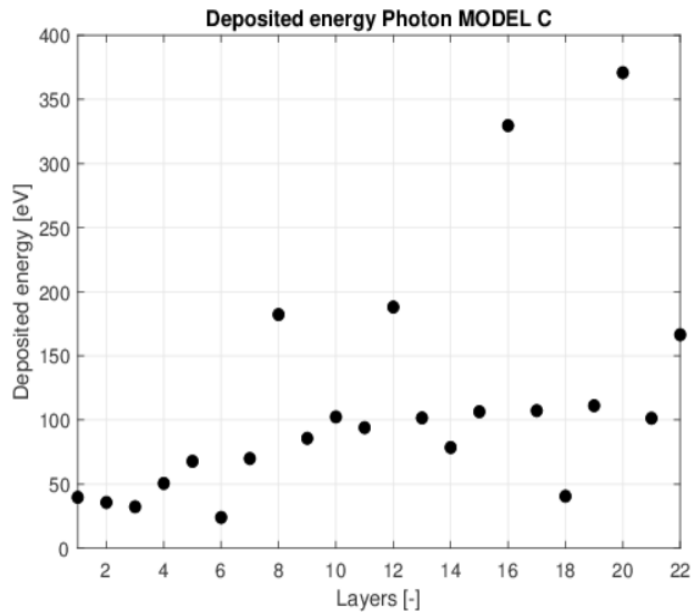


Figure 20 Deposited energy Photons MODEL C

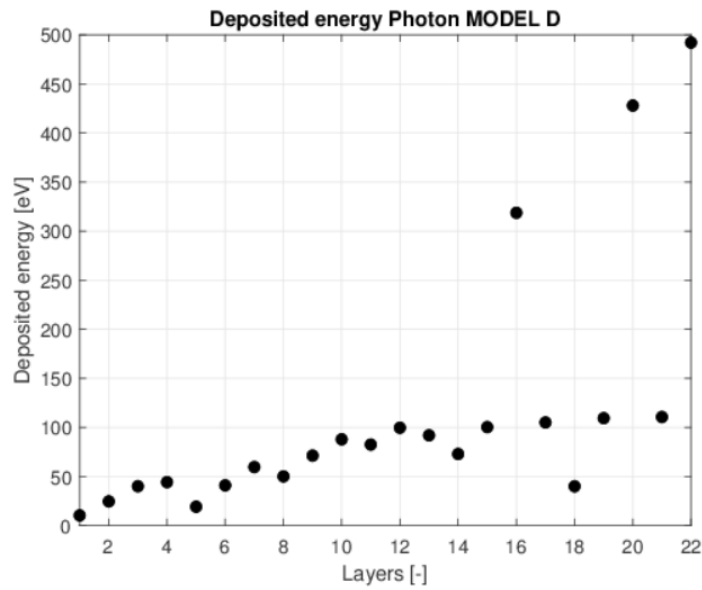


Figure 21 Deposited energy Photons MODEL D

You can also remark from these graphs, that the deposited energy in water locally reaches a higher value 110 [eV] with MODEL B (thickness of each slice 50 [μm]) than with MODEL A (thickness of each slice 10 [μm]) where the higher energy deposited in water locally is only 22 [eV].

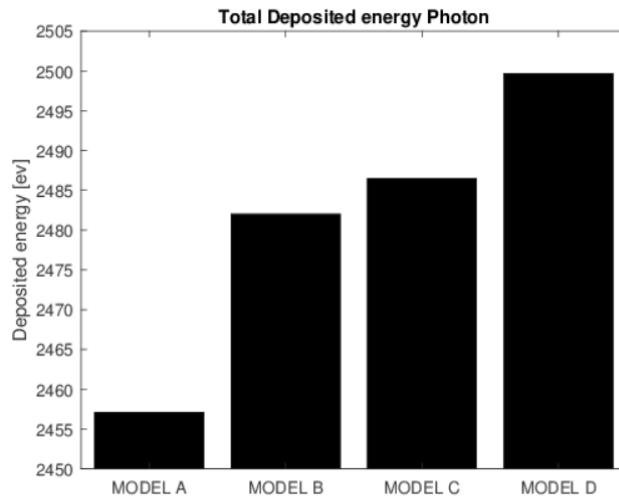


Figure 22 Total deposited energy Photons MODEL A, B, C, D

As we can see, the energy deposit is closely related to the thickness of the silicon: as it increases the energy deposit also increases.

Now, we compare the total deposited energy, evaluated in the previous cases, where we took into consideration the heterogeneous model, with the total deposited energy taking into consideration the homogeneous model (fig. 23).

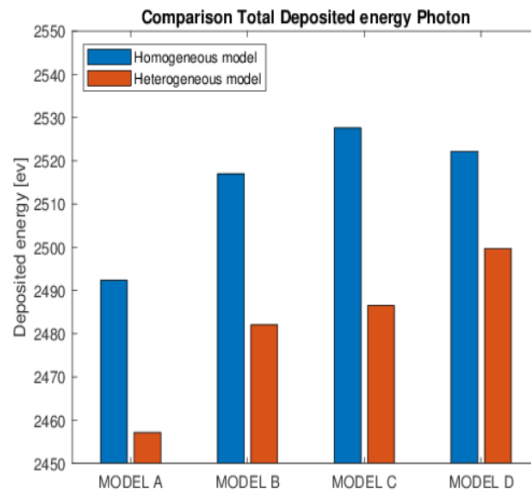


Figure 23 Comparison of Total deposited energy in the Heterogeneous and Homogeneous model

As already verified in Simulation 1, in all cases, we will have a lower energy deposit when we consider the heterogeneous model (see tab. 9).

Table 9 Percentage reduction of total deposit energy

	Percentage reduction of deposit energy in the heterogeneous model
MODEL A	1.41 %
MODEL B	1.39 %
MODEL C	1.62 %
MODEL D	0.89 %

The reduction of the total energy deposit is low, but if we consider only the energy deposited in the layers of H₂O, the reduction of energy deposited increases (fig. 24).

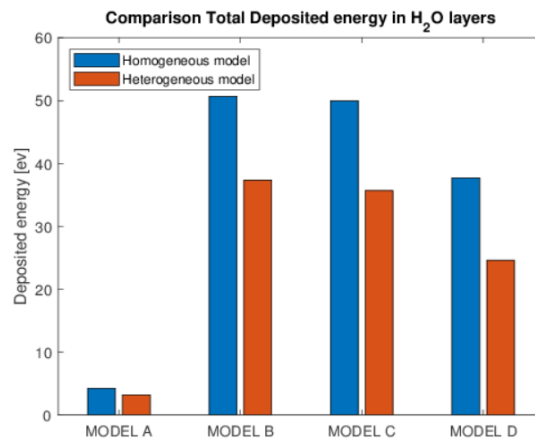


Figure 24 Comparison of Total deposited energy in H₂O in the Heterogeneous and Homogeneous model

In this case the reduction of total energy deposited in the H₂O layers is higher (see tab. 10).

Table 10 Percentage reduction of total deposit energy in H₂O

	Percentage reduction of deposit energy in the heterogeneous model
MODEL A	24.77 %
MODEL B	26.24 %
MODEL C	28.54 %
MODEL D	34.74 %

As we can see from table 10, the average reduction of deposited energy in the H₂O layers is about 30 %. As mentioned before, the homogeneous model, can be defined as "conservative". For this reason, from now on our simulations will be based exclusively on heterogeneous models.

The deposited energy of electrons (^{137}Cs , ^{90}Sr , and ^{90}Y) of each model are show in figs. 25, 26, 27 and 28.

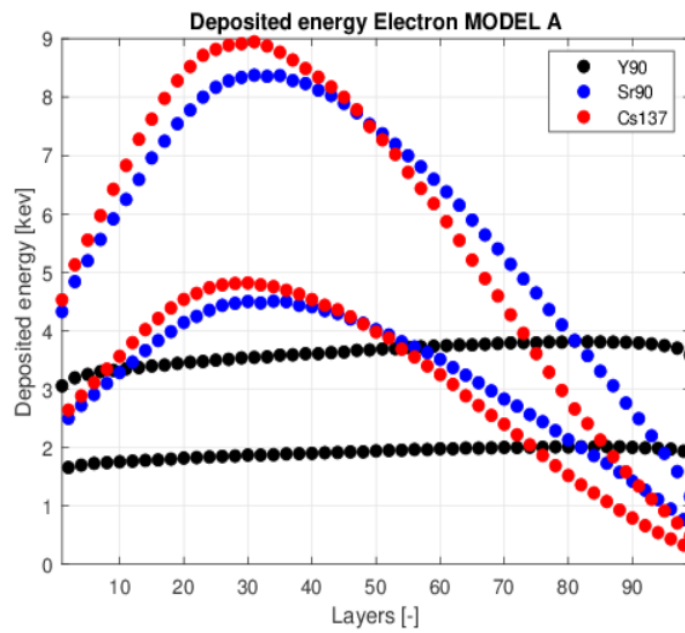


Figure 25 Deposited energy Electrons MODEL A of ^{137}Cs , ^{90}Sr , and ^{90}Y

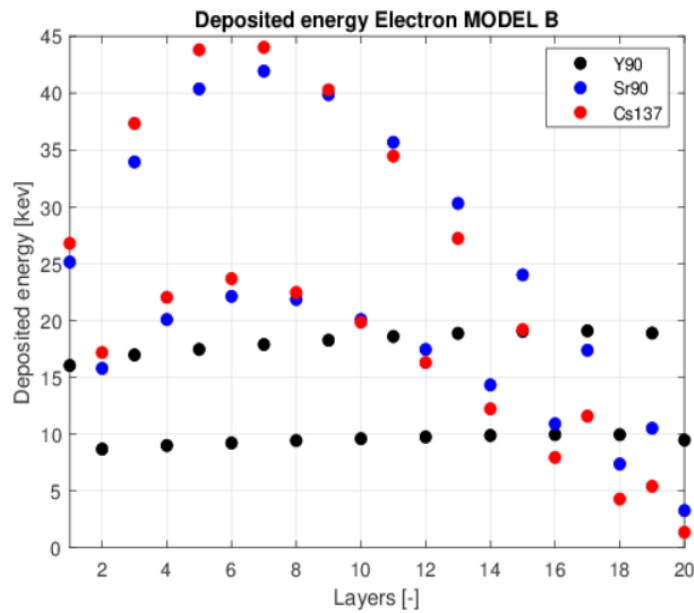


Figure 26 Deposited energy Electrons MODEL B of ^{137}Cs , ^{90}Sr , and ^{90}Y

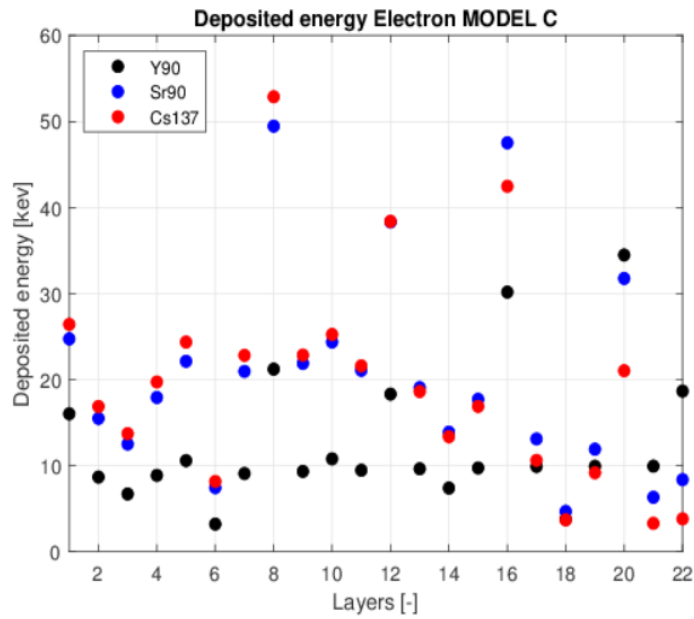


Figure 27 Deposited energy Electrons MODEL C of ^{137}Cs , ^{90}Sr , and ^{90}Y

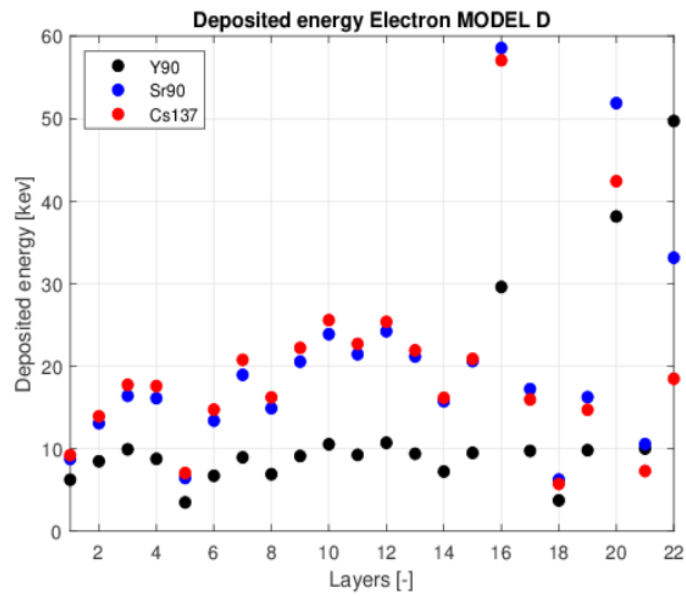


Figure 28 Deposited energy Electrons MODEL D of ^{137}Cs , ^{90}Sr , and ^{90}Y

Let us see how in the case of deposited energy of electrons (figs. 25, 26, 27, and 28), in the case of ^{90}Y we have a much lower energy deposit.

3.4 Simulation 3: “Big Layers”

Now before studying macropores filled with water, it may be useful to study the energy deposit on two large layers. First one way and then reversing them, observing what happens. The studied system is composed always of two materials, silicon and water (respectively with density $2.330 \left[\frac{g}{cm^3} \right]$ and $1.000 \left[\frac{g}{cm^3} \right]$) subjected to photonic radiation of $0.660 [MeV]$. This time it was considered a material composed alternately of two “big” cylindrical layers, total thickness $1000 [\mu m]$.

The energy deposited on each layer (figs. 29 and 30) and the total deposited energy (fig. 31) was studied, taking into account different configurations:

- MODEL A

Table 11 Configuration “big layers” MODEL A

LAYERS	MATERIAL	MODEL A thickness $[\mu m]$
1	Si	500
2	H ₂ O	500

- MODEL B

Table 12 Configuration “big layers” MODEL B

LAYERS	MATERIAL	MODEL B thickness $[\mu m]$
1	H ₂ O	500
2	Si	500

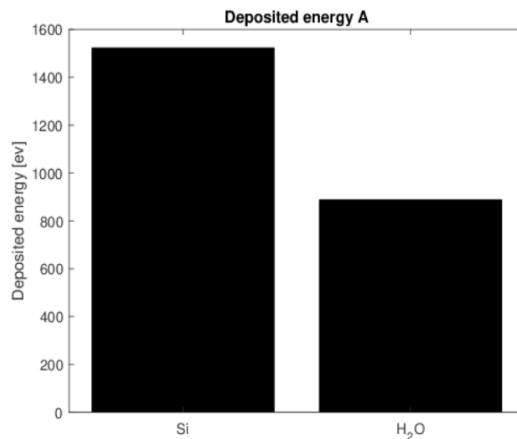


Figure 29 Deposited energy “big layers” MODEL A

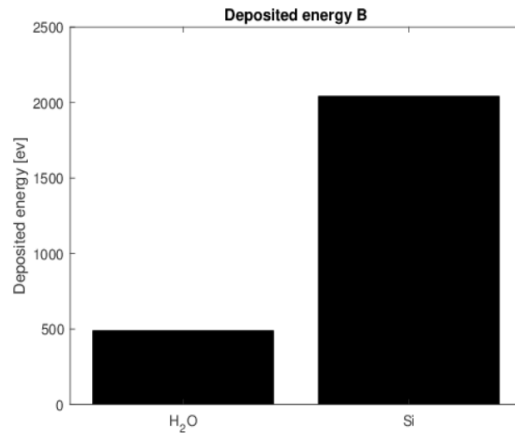


Figure 30 Deposited energy "big layers" MODEL B

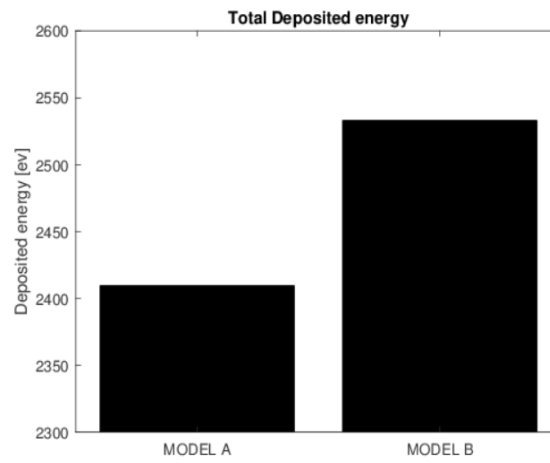


Figure 31 Total deposited energy "big layers"

It is interesting to notice that the energy deposit is greater in MODEL B, but the energy deposit in the water layer is greater in MODEL A ("conservative" model), for this reason, in the simulation of macropores we can adopt the configuration Si, H₂O, Si, H₂O and so on.

4 Simulations with TRIPOLI-4® Transport code

Now the transport calculations in this section are done using the Monte Carlo transport code TRIPOLI-4®, developed in the SERMA department in CEA Saclay. The TRIPOLI-4® code is a three-dimensional, continuous energy computer code for particle transport based on the Monte Carlo method. The code currently simulates the transport of neutrons, photons, electrons, and positrons. TRIPOLI-4® is designed for two major classes of problems, those relating to radiation shielding and those relating to reactor physics. Radiation shielding problems deal with particle propagation over long distances with many orders of magnitude of flux attenuation.

Let us consider two different modes: “ELECTRON_TOTAL_STOPPING_POWER” and default mode. Electron Total Stopping Power makes energy losses due to inelastic collisions continuous throughout the energy domain. Secondary particles are produced independently. By default, this option is not enabled. The simulation of the electromagnetic cascade takes place both in default mode and in Electron Total Stopping Power mode. Electron Total Stopping Power mode uses a simplified version of energy losses due to inelastic collisions. These energy losses are continuously evaluated over the whole energy range and the secondary particles (photons and electrons) are produced independently. This simulation corresponds to the CSDA (Continuous Slowing Down Approximation) mode. In the default calculation, electrons and photons are transported, electrons produce photons, secondary electrons are also produced (knock-on electrons), energy fluctuations (due to the production of Bremsstrahlung photons and secondary electrons "knock-on electrons") are taken into account in the calculation of energy losses. Combined with the previous option, No Electron Straggling allows disabling the fluctuations on energy losses of the particles. The CSDA mode (Continuous Slowing Down Approximation) of TRIPOLI-4® includes these fluctuations. The default mode includes more physics, but CSDA without straggling may be better suited for comparisons with other codes [18].

4.1 Simulation 1: Layers 0.005 [cm]

The studied system (fig. 32) is composed always of two materials, silicon and water (respectively with density $2.330 \left[\frac{g}{cm^3} \right]$ and $1.000 \left[\frac{g}{cm^3} \right]$) subjected to photonic (^{137}Cs) and electron radiation (^{137}Cs , ^{90}Sr , and ^{90}Y). It was considered a material composed of 20 alternating cylindrical layers, each of $50 \text{ } [\mu\text{m}]$, total thickness $1000 \text{ } [\mu\text{m}]$. Total thickness of silicon $500 \text{ } [\mu\text{m}]$ and total thickness of H_2O $500 \text{ } [\mu\text{m}]$. It is the same configuration as in chapter 3.3 MODEL B simulated with PENELOPE, and the aim is to compare the two codes.

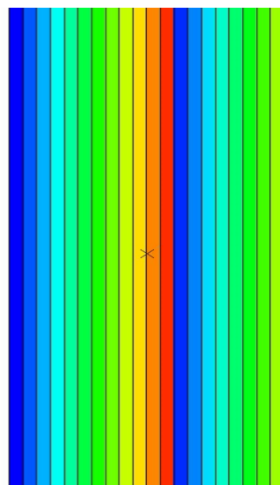


Figure 32 Configuration model of TRIPOLI-4® (parallel to x-axis)

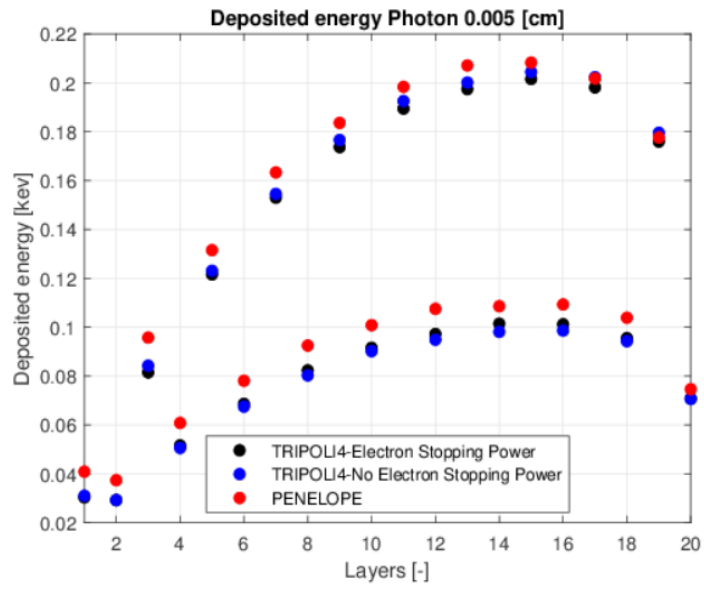


Figure 33 Comparison PENELOPE/ TRIPOLI-4® of deposited energy of Photons 0.005 [cm]

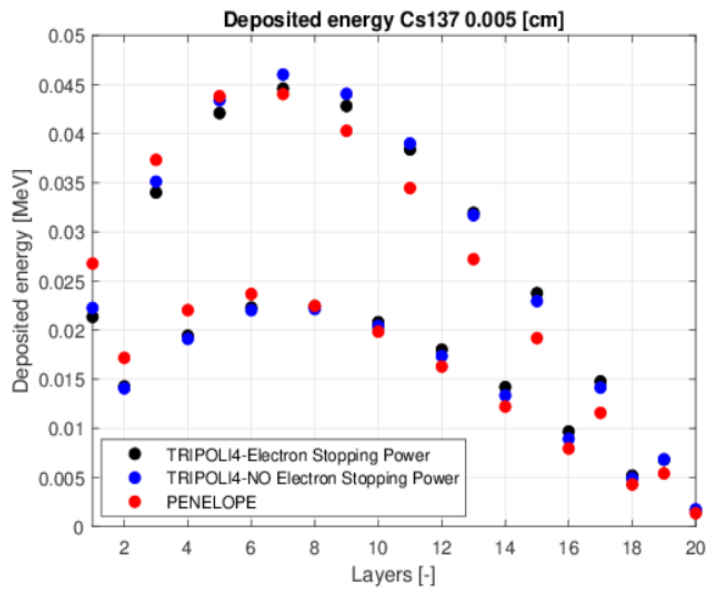


Figure 34 Comparison PENELOPE/ TRIPOLI-4® of deposited energy of ¹³⁷Cs 0.005 [cm]

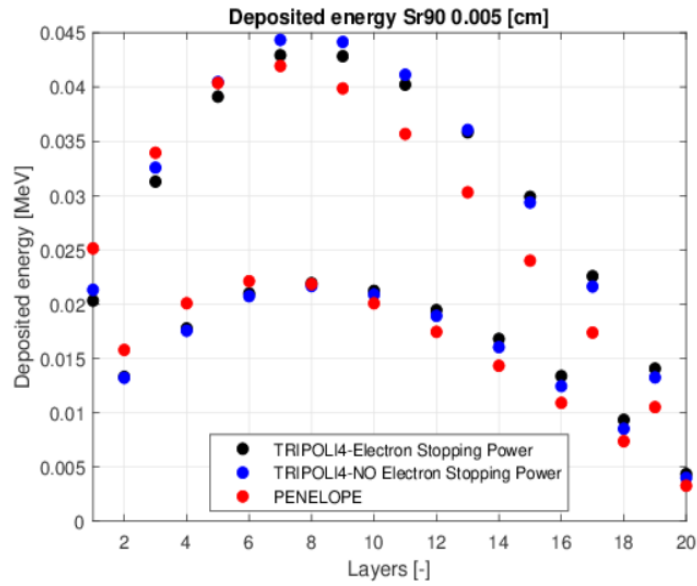


Figure 35 Comparison PENELOPE/ TRIPOLI-4® of deposited energy of ⁹⁰Sr 0.005 [cm]

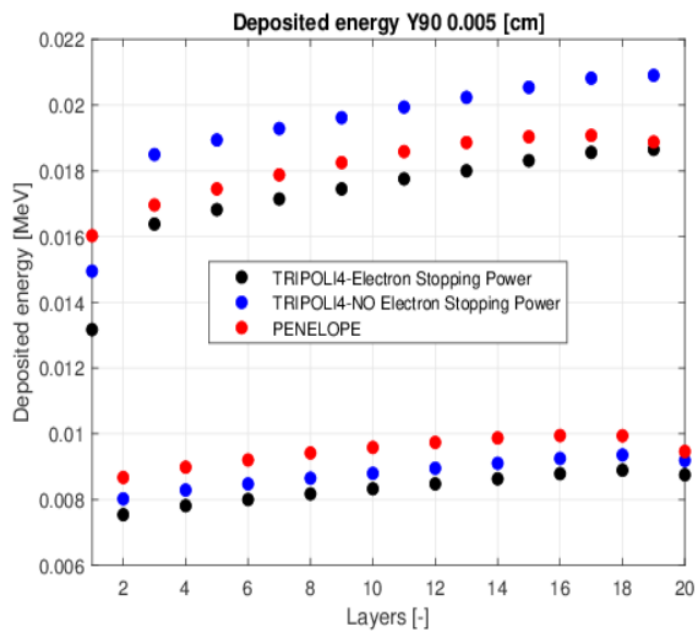


Figure 36 Comparison PENELOPE/ TRIPOLI-4® of deposited energy of ⁹⁰Y 0.005 [cm]

The energy deposition (figs. 33, 34, 35 and 36) calculations show that the default mode of TRIPOLI-4® is in good agreement with the default mode of PENELOPE. The “ELECTRON_TOTAL_STOPPING_POWER” mode of TRIPOLI-4® coincides more with the default mode of PENELOPE in the deposited energy in silicon layers. The default mode of TRIPOLI-4®, which is more detailed, deposits energy a little further into matter using a continuous approximation for collisional electron energy losses.

4.2 Simulation 2: MACROPORES Layers 0.05 [cm]

In this case we take into consideration the macropores. The studied system is composed always of two materials, silicon and water (respectively with density $2.330 \left[\frac{g}{cm^3} \right]$ and $1.000 \left[\frac{g}{cm^3} \right]$) subjected to photonic ($0.660 [MeV]$) and electron radiation (^{137}Cs , ^{90}Sr , and ^{90}Y).

It was considered a material composed of 20 alternating cylindrical layers, each of $500 [\mu m]$, total thickness $10000 [\mu m]$. Total thickness of silicon $5000 [\mu m]$ and total thickness of H_2O $5000 [\mu m]$.

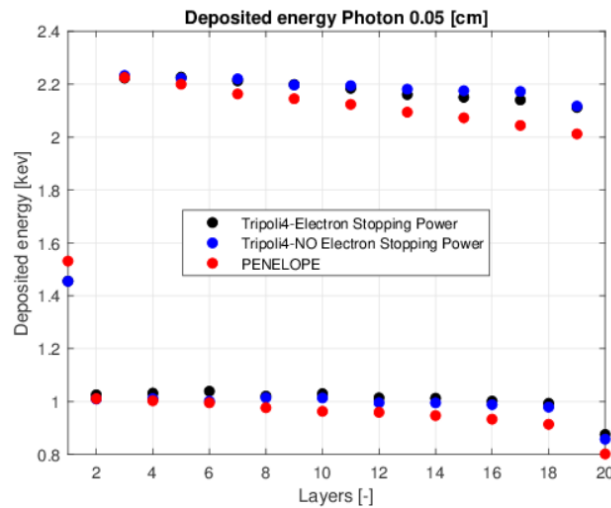


Figure 37 Comparison PENELOPE/ TRIPOLI-4® of deposited energy of Photons 0.05 [cm]

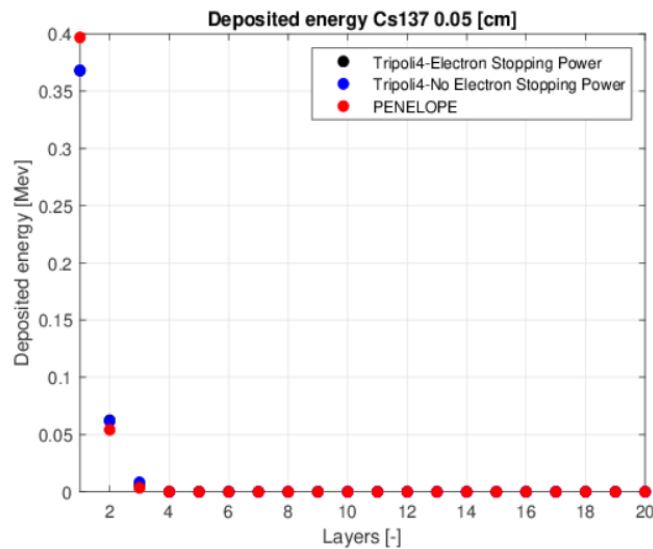


Figure 38 Comparison PENELOPE/ TRIPOLI-4® of deposited energy of ^{137}Cs 0.05 [cm]

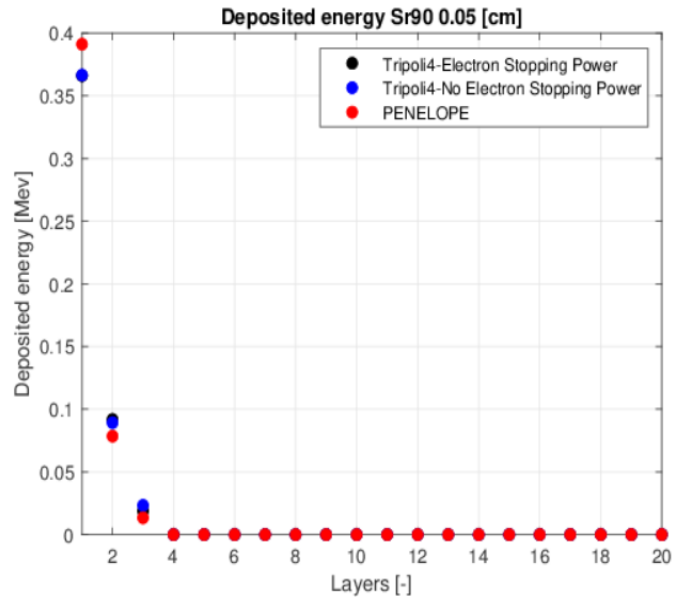


Figure 39 Comparison PENELOPE/ TRIPOLI-4® of deposited energy of ⁹⁰Sr 0.05 [cm]

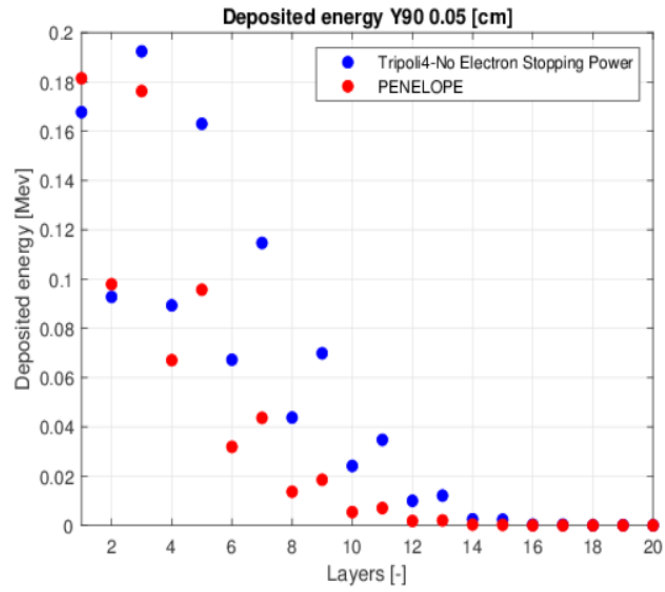


Figure 40 Comparison PENELOPE/ TRIPOLI-4® of deposited energy of ⁹⁰Y 0.05 [cm]

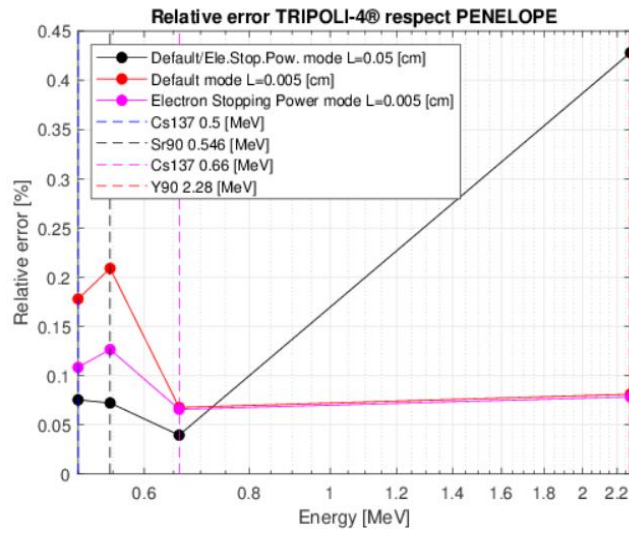


Figure 41 Relative error TRIPOLI-4®respect PENELOPE

As we can see from the graph 41, when the layers are 0.005 [cm], the greatest difference between TRIPOLI-4® and PENELOPE is at 0.500 [MeV] and 0.546 [MeV].

On the other hand, when the layers are 0.05 [cm], the error is higher at 2.280 [MeV], as we can also see from figure 40, this is mainly due to the TRIPOLI-4® bugs.

When the layers are thicker, 0.05 [cm], the behavior between TRIPOLI-4® and PENELOPE is however more similar, as could be expected.

5 Spherical Inclusions

The calculations carried out before, have been made without taking into account the position of the pores filled with “free” water in the cement. It would be interesting to study the effects of the homogenization of the geometry on the calculation of energy depositions and compare it to a more detailed calculation that takes into account the shape and the position of the pores (stochastic geometry). The generator of spherical inclusions for TRIPOLI-4® exists [19].

The basic Monte Carlo method to generate a stochastic inclusion of spheres is the random sequential addition method: basically, what we want is to have a set of randomly distributed, non-overlapping spheres knowing the radius and the portion of volume we want the spheres to occupy. These spheres will be generated inside a chosen control volume, usually a cubic box, or a parallelepiped or a cylinder or a sphere, and this volume has to be defined according to what the case of study requires (for example using a control volume coincident with the one created for the homogeneous model simulation could be a good choice, if the aim is to compare the two models).

Monodispersed Radius Spherical Inclusions uniformly distributed

In case of spherical inclusions with monodispersed radius uniformly distributed:

$$\xi = \frac{N \frac{4}{3} \pi r^3}{L_x L_y L_z} \quad (30)$$

Where:

ξ is the Packing Fraction of the inclusions, it is the ratio between the volume occupied by the spheres and the total control volume;

N is the number of the spheres;

r is the radius of the spheres;

L_x is the side of the cube.

Taken a cubic box as control volume, for spheres which cannot overlap the walls of the box, the random sampling of the first center of the inclusion is calculated according to a uniform distribution. When another set of center coordinates is sampled, it is needed to check if the last sphere overlaps with other existing ones. That is done using simple algebraic operations, in particular the distance between two points should be never smaller than the spheres diameter, and this has to be checked for each sphere. Naturally, the number of these operation increases sphere by sphere. This process ends when the number N of inclusions is reached.

5.1 TRIPOLI-4®: Spherical Inclusions Simulation

Now let us consider at a more realistic model and try to compare it with the models evaluated earlier. The studied system is composed always of two materials, silicon and water (respectively with density $2.330 \left[\frac{g}{cm^3} \right]$ and $1.000 \left[\frac{g}{cm^3} \right]$), in this case the photonic source ($0.660 [MeV]$), is the entire silicon cube that surrounds the spherical inclusions.

It was considered a silicon cube of side L , with spheres of water of radius r inside (see Tab. 13).

The MODEL A is shown in figure 42.

Table 13 Examples of spherical inclusions generation

	ξ	$L_x=L_y=L_z [cm]$	$r [cm]$	N
MODEL A	1%	2.2	0.10	25
MODEL B	1%	5.5	0.25	25
MODEL C	1%	11	0.50	25
MODEL D	1%	21	1.00	22

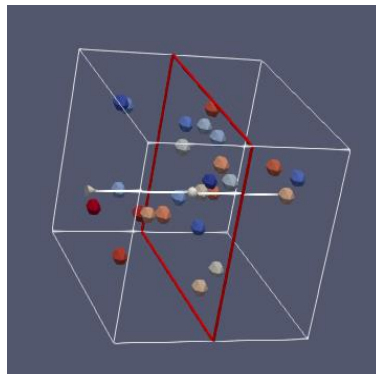


Figure 42 Paraview spherical inclusions uniformly distributed $r=0.1 [cm]$ MODEL A

5.1.1 MODEL A

In order to evaluate the total energy deposit in each model, it may be useful to simulate more than one generation of spherical inclusions. In our case, we will simulate ten random generations of spherical inclusions, then we will evaluate the average value of total deposited energy in each model, see figure 43 for MODEL A.

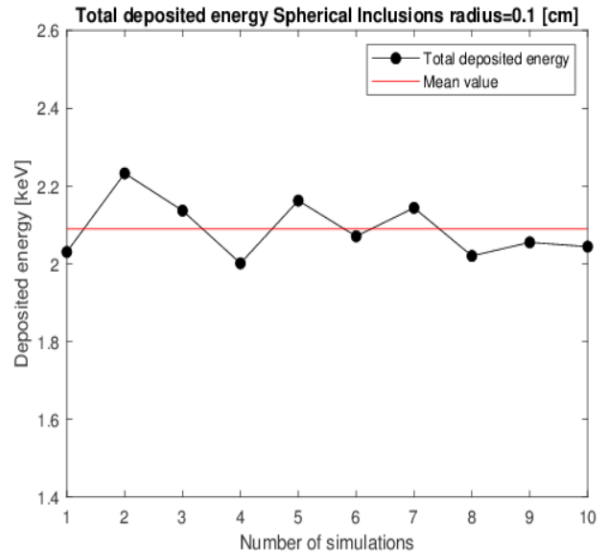


Figure 43 Total deposited energy Spherical Inclusions radius = 0.1 [cm]

The total volume of the water pores and the total average energy deposited is shown in table 14. To simulate a similar volume of water, with PENELOPE code, we have considered a cylindrical configuration with a radius of 0.4 [cm], composed alternately of 4 layers of silicon and water, each 0.1 [cm] thick.

Table 14 Comparison Volume and Total Energy deposited in Spherical Inclusions radius = 0.1 [cm] and PENELOPE

	Total volume [cm ³]	Total average energy deposited [MeV]
Spherical Inclusions	0.1047	0.0021
PENELOPE	0.1005	0.0041

5.1.2 MODEL B

The figure 44 shows the total energy deposited in ten random generations of spherical inclusions of the MODEL B and its total average energy deposited.

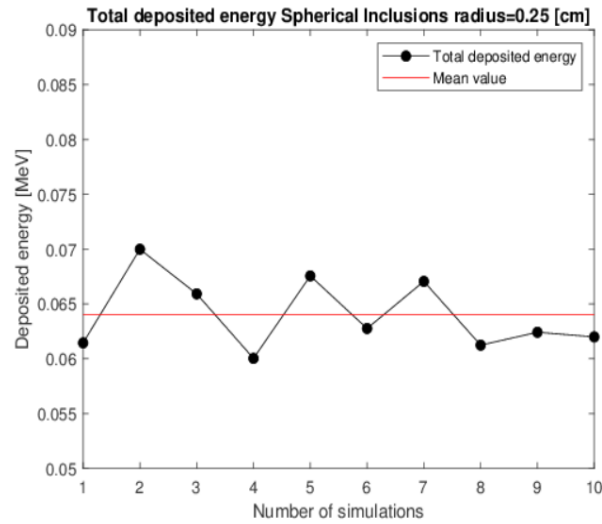


Figure 44 Total deposited energy Spherical Inclusions radius = 0.25 [cm]

Trying to simulate a similar volume of water, with PENELOPE code, we considered a material composed alternatively of 40 cylindrical layers of silicon and water, each 0.25 [cm] thick, with radius 0.32 [cm] (see tab. 15).

Table 15 Comparison Volume and Total Energy deposited in Spherical Inclusions radius = 0.25 [cm] and PENELOPE

	Total volume [cm ³]	Total average energy deposited [MeV]
Spherical Inclusions	1.6362	0.0640
PENELOPE	1.6085	0.0610

The graph shown in fig. 45 represents the energy deposits of photons in water layers, using PENELOPE code.

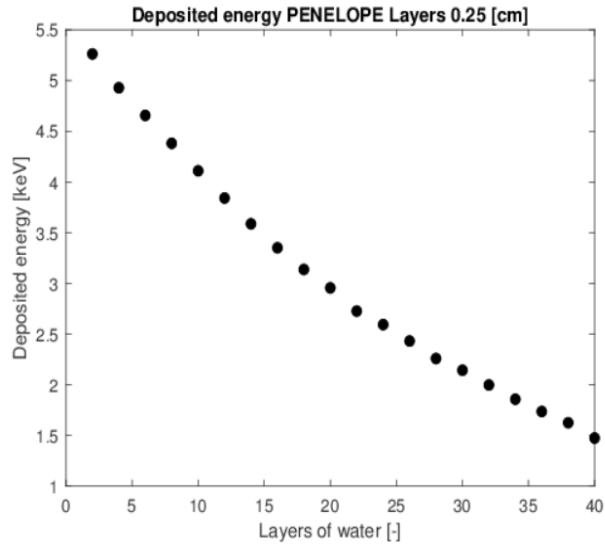


Figure 45 Deposited energy in water layers MODEL B

5.1.3 MODEL C

The figure 46 shows the total energy deposited in ten random generations of spherical inclusions of the MODEL C and its total average energy deposited.

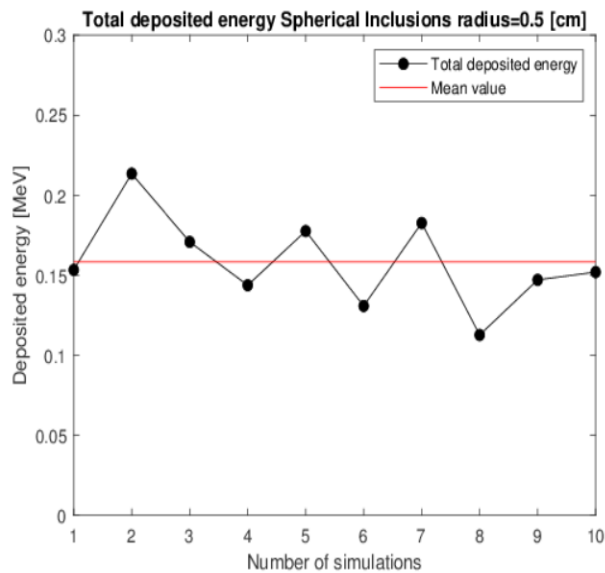


Figure 46 Total deposited energy Spherical Inclusions radius = 0.5 [cm]

Trying to simulate a similar volume of water, with PENELOPE code, we considered a material composed alternatively of 80 cylindrical layers of silicon and water, each 0.5 [cm] thick, with radius 0.45 [cm] (see tab. 16).

Table 16 Comparison Volume and Total Energy deposited in Spherical Inclusions radius = 0.5 [cm] and PENELOPE

	Total volume [cm^3]	Total average energy deposited [MeV]
Spherical Inclusions	13.09	0.1584
PENELOPE	12.72	0.0828

The graph shown in fig. 47 represents the energy deposits of photons in water layers, using PENELOPE code.

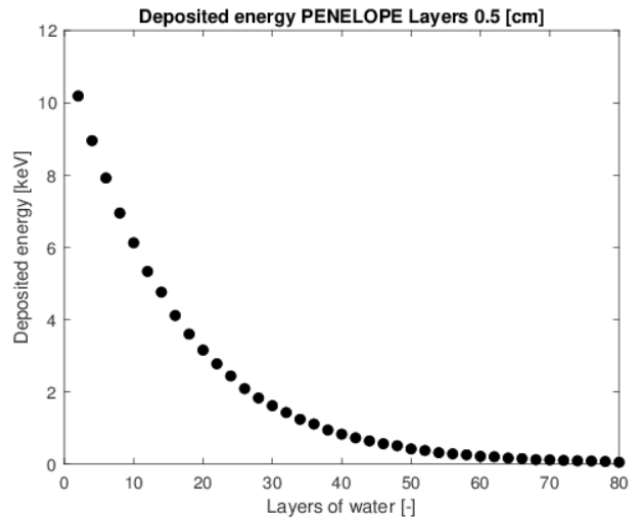


Figure 47 Deposited energy in water layers MODEL C

5.1.4 MODEL D

The figure 48 shows the total energy deposited in ten random generations of spherical inclusions of the MODEL D and its total average energy deposited.

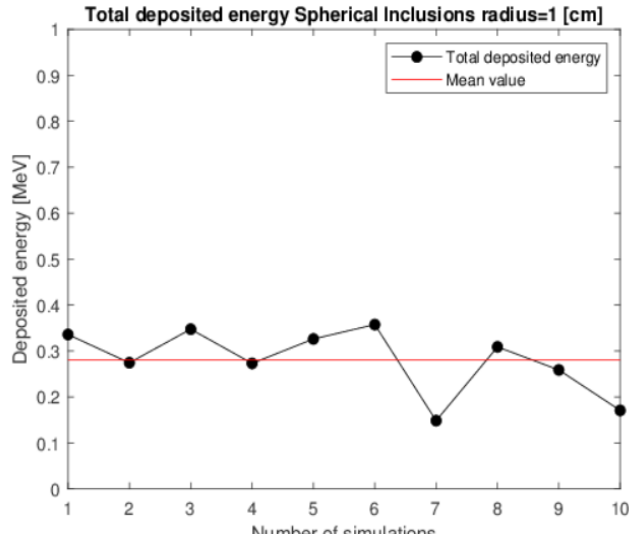


Figure 48 Total deposited energy Spherical Inclusions radius = 1 [cm]

Trying to simulate a similar volume of water, with PENELOPE code, we considered a material composed alternatively of 80 cylindrical layers of silicon and water, each 1.00 [cm] thick, with radius 0.85 [cm] (see tab. 17).

Table 17 Comparison Volume and Total Energy deposited in Spherical Inclusions radius = 1 [cm] and PENELOPE

	Total volume [cm^3]	Total average energy deposited [MeV]
Spherical Inclusions	92.1534	0.08439
PENELOPE	90.7920	0.2802

The graph shown in fig. 49 represents the energy deposits of photons in water layers, using PENELOPE code.

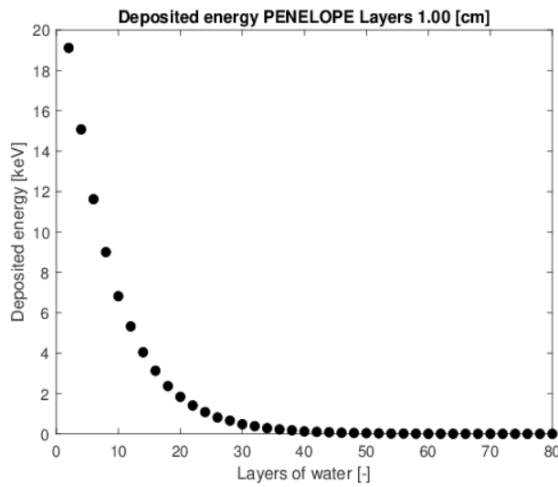


Figure 49 Deposited energy in water layers MODEL D

5.2 Comparison TRIPOLI-4[®] with Spherical Inclusions and PENELOPE

In the figure 50 we can see the comparison of the total energy deposited between TRIPOLI-4[®] with spherical inclusions and PENELOPE. We tried to evaluate the total deposited energy considering similar volumes of water.

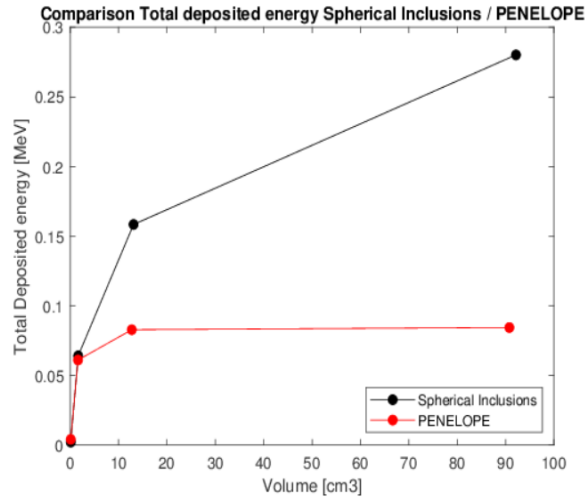


Figure 50 comparison of the total energy deposited between TRIPOLI-4[®] with spherical inclusions and PENELOPE

now let us try to calculate the relative error (fig. 51)

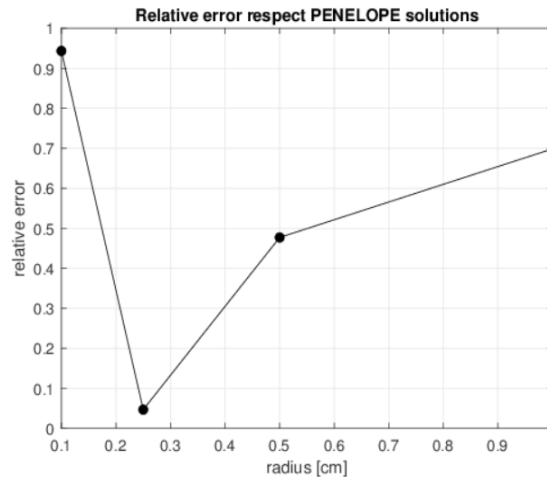


Figure 51 Relative error

As we can see, at some point, when we use a radius of 0.25 [cm], the energy deposited (in the simulations with PENELOPE) in the water pores stops increasing, and reaches an equilibrium point or saturation point. This is due to the fact that even by increasing the layers of water in our model, the energy deposited at a certain point becomes negligible, until it becomes zero.

Conclusions

In this work we have addressed the problem of energy deposition in the water pores in nuclear waste. Using computational codes based on the Monte Carlo method, PENELOPE and TRIPOLI-4[®], we simulated different types of systems, homogeneous first, then heterogeneous.

We started with a fairly simple simulation, we schematized the water pores as if they were cylinders, and subjected to external radiation from a point source. Both photons and electrons. We varied the thickness of the various layers, observing what happened in the deposition of energy, and how it varied as the thickness of the silicon and water layers varied.

We compared the results obtained with PENELOPE, with those obtained with TRIPOLI-4[®], verifying that they were consistent.

Finally, we wanted to simulate a case closer to reality because, the calculations carried out before have been made without taking into account the position of the pores filled with “free” water in the cement. We therefore used a spherical inclusion geometry, using an algorithm based on the Monte Carlo method, in order to generate a stochastic inclusion of spheres.

From what we can see, the simple method used at the beginning, i.e. a system formed by alternating layers of water and silicon, works well if we want to simulate the energy deposit in the micropores of water in concrete, but it starts to give some problems when we want simulate the energy deposit in the macropores of water in concrete. This is mainly due to the fact that even as the layers of water and silicon increase, at some point the energy deposit tends to zero.

It must also be taken into account that increasing the layers by a lot does not make much sense, as we move a little away from the real model we want to simulate.

For this reason, before simulating a physical model for the deposition of energy in the pores of water in concrete, it is necessary to take into account the size of the water pores, and then make the necessary considerations on which could be the physical model that best suits to our problem.

References

- [1] P. Results of a Coordinated Research, "The Behaviours of Cementitious Materials in Long Term Storage and Disposal of Radioactive Waste," IAEA, Vienna, 2013.
- [2] ANDRA Agence Nationale pour la gestion des Déchets Radioactifs, "F2-3-01: Colis de coques et embouts cimentés, en fûts métalliques (Orano/La Hague)," Inventaire National Des Matières et Déchets Radioactifs, France, 2016.
- [3] ANDRA Agence Nationale pour la gestion des Déchets Radioactifs, "F2-3-13: Colis de fines et résines du silo HAO (Orano/La Hague)," Inventaire National Des Matières et Déchets Radioactifs, France, 2016.
- [4] M. M. C. Canut, "Pore structure in blended cement pastes," Department of Civil Engineering, Technical University of Denmark, 2011.
- [5] H. M. Jennings, "A model for the microstructure of calcium silicate hydrate in cement paste," *Cement and Concrete Research*, 30, 1999.
- [6] P. J. McDonald, V. Rodin and A. Valori, "Intra-C–S–H sheet pores and inter-C–S–H particle gel pores," 2010.
- [7] T. C. Powers, "Physical properties of cement paste," Research and Development Laboratories of the Portland Cement Association, Bulletin 154, 1960.
- [8] A. M. Kjeldsen and M. R. Geiker, "On the interpretation of flow temperature calorimetry data," *Material and Structure* 41, 2008.
- [9] Z. Sun and G. W. Scherer, "Pore size and shape in mortar by thermoporometry," *Cement and Concrete Research* 40, 2010.
- [10] K. K. Aligizaki, "Pore structure of cement-based materials: testing, interpretation and requirements.," 2006.
- [11] T. B. Hansen, J. Thrylsøe, P. A. Simmelsgaard and M. T. Jespen, "Experimental characterization of porous materials," Aalborg Portland Cement, 2000.
- [12] G. H. Michler, "Electron microscope for polymers," Springer-Verlag, Heidelberg, 2008.
- [13] E. Gallucci, K. Scrivener, A. Groso, M. Stampanoni and G. Margaritondo, "3D experimental investigation of the microstructure of cement pastes using synchrotron X-ray microtomography (μ CT)," *Cement and Concrete Research* 37, 2007.
- [14] V. Kocaba, "Development and evaluation of methods to follow microstructural development of cementitious systems including slags," Materials Department, Lausanne, École Polytechnique Fédérale de Lausanne, 2009.
- [15] K. Scrivener and P. L. L. and Pratt, "Characterisation of portland cement hydration, by electron optical techniques," *Electron microscopy of materials. Mater Res Soc Symp Proc.*, 1983.
- [16] M. Berger, J. Coursey and M. Zucker, "ESTAR, PSTAR, and ASTAR: Computer Programs for Calculating Stopping-Power and Range Tables for Electrons, Protons, and Helium Ions," National Institute of Standards and Technology, Gaithersburg, 2000.
- [17] P. Rotureau, "Etude de la radiolyse de l'eau en milieu poreux," Doctoral dissertation, Université d'Evry-Val d'Essonne, 2004.
- [18] E. Brun, F. Damian, C. Diop, E. Dumonteil, F. Hugot, C. Jouanne, Y. Lee, F. Malvagi, A. Mazzolo, O. Petit, J. Trama, T. Visonneau and A. Zoia, "Tripoli-4[®]," CEA, EDF and AREVA reference Monte Carlo code, France, 2015.
- [19] C. Larmier, "Stochastic particle transport in disordered media: beyond the Boltzmann equation," Doctoral dissertation, Université Paris-Saclay, 2018.
- [20] [Online]. Available: <http://www3.med.unipmn.it/arneodo/corso/radioprotezione/lezioni/lezione1-2018.pdf>.

- [21] A. Bonin and F. Hugot, "Contribution à la V&V électrons de TRIPOLI-4[®]," CEA/DEN/DANS/DM2S/SERMA/LTSD/NT/14-5732/A, Paris, 2014.
- [22] E. Browne and R. Firestone, "Table of Radioactive Isotopes (John Wiley & Sons, New York, 1986), recent Nuclear Data Sheets, and X-ray and Gamma-ray Standards for Detector Calibration," IAEA-TECDOC-619, 1991.
- [23] F. Salvat, J. Fernandez-Varea, E. Acosta and J. Sempau, "PENELOPE-A Code System for Monte Carlo Simulation of electron and Photon Transport," Nuclear Energy Agency, Universitat de Barcelona, Spain, 2001.
- [24] A. Valori, "Characterisation of cementitious materials by ¹H NMR," Department of Physics, University of Surrey, 2009.
- [25] R. Feldam, "Pore structure damage in blended cements caused by mercury intrusion," Journal of the American Society Journal of the American Society, 1984.
- [26] O. Cebeci, "The Intrusion of Conical and Spherical Pores," Journal of Colloid and Interface Science 78, 1980.
- [27] "Monte Carlo Simulation of Radiation Transport," Agen-689 Advances in Food Engineering.